

First observation of increased DT yield over prediction due to addition of hydrogen

Cite as: Phys. Plasmas **28**, 012707 (2021); <https://doi.org/10.1063/5.0030852>

Submitted: 25 September 2020 . Accepted: 31 December 2020 . Published Online: 22 January 2021

 Y. Kim,  H. W. Herrmann,  N. M. Hoffman,  M. J. Schmitt, G. Kagan, A. M. McEvoy,  A. B. Zylstra,  J. M. Smidt,  S. Gales,  A. Leatherland, M. Rubery,  M. Gatu Johnson,  J. A. Frenje,  V. Yu Glebov, and C. Forrest

COLLECTIONS

 This paper was selected as an Editor's Pick



[View Online](#)



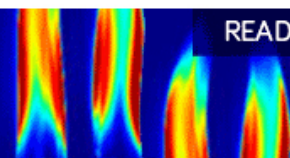
[Export Citation](#)



[CrossMark](#)

AIP Advances
Fluids and Plasmas Collection















READ NOW



First observation of increased DT yield over prediction due to addition of hydrogen

Cite as: Phys. Plasmas **28**, 012707 (2021); doi: [10.1063/5.0030852](https://doi.org/10.1063/5.0030852)
Submitted: 25 September 2020 · Accepted: 31 December 2020 ·
Published Online: 22 January 2021



Y. Kim,^{1,a)}  H. W. Herrmann,¹  N. M. Hoffman,¹  M. J. Schmitt,¹  G. Kagan,^{1,b)}  A. M. McEvoy,¹  A. B. Zylstra,^{1,c)} 
J. M. Smidt,¹  S. Gales,²  A. Leatherland,²  M. Rubery,²  M. Gatu Johnson,³  J. A. Frenje,³  V. Yu Glebov,⁴ 
and C. Forrest⁴

AFFILIATIONS

¹Los Alamos National Laboratory, Los Alamos, New Mexico 87545, USA

²Atomic Weapons Establishment, Aldermaston, Reading, Berkshire RG7 4PR, United Kingdom

³Plasma Science and Fusion Center, Massachusetts Institute of Technology, Cambridge, Massachusetts 02139, USA

⁴Laboratory for Laser Energetics, University of Rochester, Rochester, New York 14623, USA

^{a)}Author to whom correspondence should be addressed: yhkim@lanl.gov

^{b)}Present address: Imperial College, London SW72AZ, United Kingdom.

^{c)}Present address: Lawrence Livermore National Laboratory, Livermore, California 94550, USA.

ABSTRACT

In a number of reported instances, implosions utilizing fuel mixtures have resulted in anomalously low fusion yields below those predicted by radiation-hydrodynamics simulations. Inter-species ion diffusion has been suggested as a possible cause of the observed yield degradation in fuel mixture implosions. An experimental platform utilizing hydro-equivalent deuterium–tritium (DT), deuterium–tritium–hydrogen (DTH), and deuterium–tritium–helium3 (DT³He) capsule implosions was developed to determine whether the inter-species ion diffusion theory may describe the resulting fuel mixture implosion behavior. The implosion experiments were performed at the Omega laser facility. X-ray images and shell areal density diagnostics results show that the hydro-equivalent three capsules (DT, DTH, and DT³He) have similar compression behavior. However, nuclear yield deviation was observed from the scaling determined using a fusion yield formula. In the DT³He mixture, a reduced yield of a factor of 0.65 ± 0.13 was observed, which is similar to a yield reduction observed in D³He mixture by Rygg *et al.* (i.e., Rygg effect). In contrast, in the DTH mixture, a factor of 1.17 ± 0.15 yield increase was observed, which we named the inverse Rygg effect. The yield increase observed in the DTH mixture is consistent with the inter-species ion diffusion theory where lighter H diffuses away from the core and concentrated DT in the core produces higher yield. An inter-species ion diffusion model, the Zimmerman–Paquette–Kagan–Zhdanov model, implemented in a Lagrangian radiation-hydrodynamics fluid code, was also used to analyze the present data, without the need to assume hydrodynamic equivalence of the capsules, but it does not completely explain the DTH or DT³He capsules although its effects are in the correct direction. Simulation-based Bayesian inference was used in the latter analysis to quantify the uncertainty in the numerical simulations. The simulation-based analysis resulted in an inferred Rygg-effect yield decrease factor of 0.91 ± 0.02 for the DT³He mixture, and an inferred inverse-Rygg yield increase factor of 1.21 ± 0.04 for the DTH mixture, based on simulations ignoring ion diffusion.

Published under license by AIP Publishing. <https://doi.org/10.1063/5.0030852>

I. INTRODUCTION

A binary mixture of equimolar deuterium (D) and tritium (T) is often used in inertial confinement fusion (ICF) experiments because this mixture is known to maximize fusion yield. A variety of other fuel species and mixtures are utilized to study specific aspects of the implosion process in order to optimize target and driver designs. For example, the use of D and ³He as a surrogate for deuterium–tritium (DT) provides a means of characterizing capsule performance while

minimizing complications associated with tritium fills or handling. In addition, gaseous dopants with a higher atomic number such as argon or krypton may be mixed with either DD or D³He to provide x-ray and nuclear diagnostic signatures. In a number of reported instances, implosions utilizing fuel mixtures have resulted in anomalously low fusion yields below those predicted by radiation-hydrodynamic simulations.^{1–9} For example, in 2004, Lindl *et al.* carried out indirect-drive implosions with D₂ filled capsules with and without the addition of

trace quantities of argon gas.¹ Observed DD fusion yields for the argon-doped capsules were lower than the calculated 1D predictions by over a factor of two more than the observed argon-free capsule yields. In 2006, Rygg *et al.* studied direct-drive capsule implosions with a variety of D³He target fill mixtures.² The D³He mixtures were all carefully chosen to maintain hydrodynamic equivalency (same total fuel mass and total particle density including electrons). Equimolar D³He implosions were observed to produce about 50% lower DD fusion yield, relative to expected, than pure D₂ gas fill implosions or implosions with mostly ³He fill (7% D), indicating that anomalous yield degradation is highly dependent on the relative fuel concentrations. In this paper, we will name the observed yield reduction over prediction due to ³He addition as the Rygg effect following the author of the Ref. 2 publication.

Leading ICF simulation codes (HYDRA, RAGE, LILAC, etc.) utilizing single fluid and average-ion approximations did not predict the observed yield reduction for fuel mixtures, which brought the validity of these simplifications into question. A plasma barodiffusion¹⁰ and an inter-species ion diffusion^{11,12} have been suggested as possible causes of the observed yield degradation in fuel mixture implosions. According to those theories, strong thermodynamic forces, e.g., concentration-, pressure-, electric potential-, and temperature-gradients, in an imploding capsule may drive significant inter-species diffusion (largely dependent on ion mass, charge, and relative concentrations) leading to ion species separation. For example, applying those theories to an equimolar D³He implosion results in ³He ions being concentrated at the core because lighter, lower charged D diffuses outward. Depletion of D in the hot core where the fusion cross sections are largest leads to a degradation of the DD fusion yield as compared to that of a pure DD implosion.

If the Rygg effect (i.e., yield reduction in D³He implosion) suggests that heavier atoms remain in the hot center of the hot spot while lighter atoms move to the cooler edge, the opposite yield increase should be observed in DH mixture, where heavier D atoms will be concentrated in the hot spot. The idea of testing a DH mixture was suggested by Amendt *et al.*¹³ and one may name an increase in yield from fuel mixture as the Amendt effect or the inverse Rygg effect. However, it is not possible to create a hydrodynamically equivalent fuel between DH and pure D₂ because two hydrogen atoms are needed for every replaced deuterium atom for mass equivalence, which doubles the total particle density (including electrons) and breaks the fuel hydro-equivalency. However, this problem can be avoided by using three species: a DT fuel can be made hydrodynamically equivalent to both a DT³He and deuterium–tritium–hydrogen (DTH) fuel. In the past, three species mixtures (DT³He or DTH) have been used in the ICF research. In 2008, Herrmann *et al.* observed anomalous yield reduction when ³He was added to DT fuel mixture.³ In 2015, Meezan *et al.*¹⁴ reported a DTH fuel mixture in a cryogenic layer implosion fielded at the National Ignition Facility.¹ A three species diffusion remains more complicated to understand than a two species diffusion; however, keeping one species to a small percentage compared to the other two, it may be approximated as a two species diffusion. Employing tritium gives us additional diagnostic benefits, for example, the ratio of yields (DD/DT or TT/DT) can be employed to compare between all three of the fuels. The yield ratio depends weakly on the

shot-to-shot variation, whereas absolute yield (e.g., DD yield in D³He capsule or DT yield in DT³He capsule) requires a control shot to compare with (e.g., DD capsule as a control shot for D³He capsule or DT capsule as a control shot for DT³He capsule).

With this motivation, an experimental platform was developed to observe if the inverse Rygg effect (or Amendt effect) might generate enhanced DT yields in DTH capsule comparison to DT fills, or if not, rule-out the inverse Rygg effect. DT³He filled target implosions (hydro-equivalent to the DT and DTH fills) were additionally fielded to confirm the DT yield reduction phenomenon observed by Herrmann *et al.* using a non-hydro-equivalent DT³He capsule in 2008.³

II. HYDRO-EQUIVALENT MIXING

For the experiments reported herein, the relative fuel species concentrations were carefully chosen to control the diffusion ratios between specific pairs of fuel species (introduced in Refs. 11 and 12) in an attempt to accentuate the inter-species diffusion phenomena of interest. According to the inter-species ion diffusion theory, equimolar DT target implosions for the DT mixture have nearly maximized diffusion ratios (see Fig. 2 of Ref. 11). For fixed values of the pressure, potential, and concentration gradients, the predicted ion separation between D and T will be maximized when the diffusion ratios are maximized. Observations of anomalously high(low) TT(DD) neutron yields in DT filled direct-drive implosions by Casey *et al.*¹⁵ were attributed to an increase(decrease) of the T(D) concentration in the core due to ion separation. The implosions reported by Casey *et al.* utilized capsule fills with a T:D ratio of ~ 0.75 and ~ 0.62 . In contrast, fill pressures of D₂ (X) and T₂ (U) were chosen for this experiment to minimize diffusion ratios and to be 8.9 atm ($=X_o$, initial D₂ pressure) and 0.5 atm ($=U_o$, initial T₂ pressure), respectively, while DT filled capsules acted as a control. Consequently, the atomic fraction of D (f_D) was about 0.95 [$=X_o/(X_o + U_o)$] and the atomic fraction of T (f_T) was about 0.05 [$=U_o/(X_o + U_o)$], which is referred to as the “95/5 DT” capsules in this paper. According to Ref. 11, the DT diffusion ratios in the 95/5 DT capsule are $\sim 20\%$ of their maximum values, leading to the prediction of a relatively low inter-species diffusion between D and T. As defined in Rygg *et al.*,² the average nuclear mass (\bar{m}) in the 95/5 DT mixture can be expressed as $\bar{m} = m_p(2f_D + 3f_T) = m_p(2X_o + 3U_o)/(X_o + U_o)$, where m_p is the proton mass. Therefore, the number densities of D (n_D) and the number density of T (n_T) are

$$\begin{aligned} n_D^{DT} &= f_D n = f_D \frac{\rho}{\bar{m}} = \left(\frac{X_o}{2X_o + 3U_o} \right) \frac{\rho}{m_p}, \\ n_T^{DT} &= f_T n = f_T \frac{\rho}{\bar{m}} = \left(\frac{U_o}{2X_o + 3U_o} \right) \frac{\rho}{m_p}, \end{aligned} \quad (1)$$

where n is the total number density, and ρ is the mass density. The expected DT neutron yield is determined by the spatial and temporal integral of the product of reactant densities times the temperature-dependent thermal reactivity of the DT nuclear reaction [adopted from Eq. (4) in Ref. 2]

$$Y_{DT} = \int n_D(r, t) n_T(r, t) \langle \sigma v(T_i(r, t)) \rangle_{DT} dr^3 dt, \quad (2)$$

where Y_{DT} is the DT neutron yield and $\langle \sigma v \rangle$ is the local thermal reactivity averaged over a Maxwellian ion velocity distribution with

temperature T_i . Therefore, the DT yields from the 95/5 DT capsule (Y_{DT}^{DT}) can be re-expressed

$$Y_{DT}^{DT} = \frac{X_0 U_0}{(2X_0 + 3U_0)^2} \int \frac{\rho^2(r, t)}{m_p^2} \langle \sigma v(T_i(r, t)) \rangle_{DT} dr^3 dt. \quad (3)$$

“DTH” filled capsules that are hydro-equivalent to the DT fills were accomplished by exchanging two D atoms from X_0 for each HT added. The resulting fill pressures of D_2 (X) and H_2 (Z) were therefore described by $X = X_0 - 2Z$, and the fill pressure of T_2 (U) was determined by $U = U_0 + Z$. So, for the DTH case, $f_D = (X_0 - 2Z)/(X_0 + U_0)$, $f_T = (U_0 + Z)/(X_0 + U_0)$, $f_H = Z/(X_0 + U_0)$, and $\bar{m} = m_p(2f_D + 3f_T + f_H) = m_p(2X_0 + 3U_0)/(X_0 + U_0)$, identical to the case for DT filled capsules, where f_H is the hydrogen fraction by atom percent in the DTH capsule. Therefore, n_D and n_T of DTH capsule are

$$n_D^{DTH} = \left(\frac{X_0 - 2Z}{2X_0 + 3U_0} \right) \frac{\rho}{m_p}, \quad n_T^{DTH} = \left(\frac{U_0 + Z}{2X_0 + 3U_0} \right) \frac{\rho}{m_p}. \quad (4)$$

Therefore, the DT yields from the DTH capsule (Y_{DT}^{DTH}) can be re-expressed

$$Y_{DT}^{DTH} = \left(\frac{X_0 - 2Z}{2X_0 + 3U_0} \right) \left(\frac{U_0 + Z}{2X_0 + 3U_0} \right) \int \frac{\rho^2(r, t)}{m_p^2} \langle \sigma v(T_i(r, t)) \rangle_{DT} dr^3 dt. \quad (5)$$

The DTH capsules were filled with H_2 (Z) = 4.2 atm, T_2 (U) = 4.7 atm, and D_2 (X) = 0.5 atm which results in $f_H \sim Z/(X_0 + U_0) = 0.45$ and $f_T \sim (U_0 + Z)/(X_0 + U_0) = 0.5$. These near equal fractions of H and T may lead to a near maximized inter-species HT diffusion ratio. If the DTH and 95/5 DT capsules are hydrodynamically equivalent, the yield ratio produces the following result:

$$\frac{Y_{DT}^{DTH}}{Y_{DT}^{DT}} = \frac{(X_0 - 2Z)(U_0 + Z)}{X_0 U_0} = 0.53. \quad (6)$$

If the inverse Rygg effect exists, the actual or observed yield ratio will be larger than 0.53.

Similarly, “DT^{3He}” filled capsules that are hydro-equivalent to the DT fill were created by exchanging three D atoms from X_0 for two ^{3He} atoms, or, equivalently, three D_2 diatomic molecules for four ^{3He} monatomic molecules. The resulting fill pressures of D_2 (X) and ^{3He} (W) were therefore adjusted by $X = X_0 - \frac{3}{4}W$, using the formula given by Rygg *et al.*² For the DT^{3He} case, $f_D = 3X/(X + 2X_0 + 3U_0)$, $f_T = 3U_0/(X + 2X_0 + 3U_0)$, $f_{3He} = 2(X_0 - X)/(X + 2X_0 + 3U_0)$, and $\bar{m} = m_p(2f_D + 3f_T + 3f_{3He}) = m_p(3 - f_D)$, where f_{3He} is the ^{3He} fraction by atom percent in the DT^{3He} capsule. Therefore, n_D and n_T of DT^{3He} capsule are

$$n_D^{DT3He} = \left(\frac{X}{2X_0 + 3U_0} \right) \frac{\rho}{m_p}, \quad n_T^{DT3He} = \left(\frac{U_0}{2X_0 + 3U_0} \right) \frac{\rho}{m_p}. \quad (7)$$

Therefore, the DT yields from the DT^{3He} capsule (Y_{DT}^{DT3He}) can be re-expressed

$$Y_{DT}^{DT3He} = \left(\frac{X}{2X_0 + 3U_0} \right) \left(\frac{U_0}{2X_0 + 3U_0} \right) \int \frac{\rho^2(r, t)}{m_p^2} \langle \sigma v(T_i(r, t)) \rangle_{DT} dr^3 dt. \quad (8)$$

The DT^{3He} capsule consisted of ^{3He} (W) = 7.1 atm, D_2 (X) = 3.58 atm, and T_2 (U) = 0.5 atm, which results in $f_D \sim 3X/(X + 2X_0$

+ $3U_0) = 0.47$ and $f_{3He} \sim 2(X_0 - X)/(X + 2X_0 + 3U_0) = 0.47$. The equal fractions of ^{3He} and D will generate strong D-^{3He} inter-species diffusion. If the DT^{3He} and 95/5 DT capsules are hydrodynamically equivalent, the yield ratio produces the following result:

$$\frac{Y_{DT}^{DT3He}}{Y_{DT}^{DT}} = \frac{X}{X_0} = 0.40. \quad (9)$$

If the Rygg effect exists, the actual or observed yield ratio will be smaller than 0.40.

III. EXPERIMENTAL SETUP

Three types of fuel mixtures were contained in spherical glass (SiO_2) shells fabricated by General Atomics. The outer diameter and wall thickness of 11 capsules are plotted in Fig. 1. The outer diameter ranges from 1091 to 1167 μm and wall thickness from 4.04 to 4.64 μm , which is a typical range of variation. The surface uniformity of the glass shells was not measured before the experiment. However, the target team at General Atomics measured a variation of 4π -wall-thickness, which ranged from 0.1 μm to up to 0.3 μm . We selected all 11 capsules which have 0.1 μm 4π -wall-thickness. In this paper, the capsules were grouped by the wall thickness, where the distribution of thin-shell group is $4.06 \pm 0.02 \mu m$, middle-shell group is $4.26 \pm 0.04 \mu m$, and thick-shell group is $4.61 \pm 0.04 \mu m$. In the thin-shell group, one shell was filled with DT and the other two shells with DT^{3He} at the Lawrence Livermore National Laboratory. In the middle-shell group, two shells were filled with DT, two shells with DTH, and two shells with DT^{3He}. In the thick-shell group, one shell was filled with DT and the other with DTH. Table I shows as-shot conditions for the 11 capsules. Pressures shown in the table are the estimated values at the shot time, while taking into account (1) gas leakages based on the amount of time each target was exposed to room temperature prior to shot time and (2) measured permeation half-lives. Gas pressures at shot time were in good agreement with requested fill pressures and were within 96%–114%. Table IV shows the requested pressures, fill pressures (over-pressured to compensate leak), and the percentage of as-shot pressures to requested pressures.

The implosion experiments of the DT, DTH, and DT^{3He} capsules were performed at the Omega laser facility.¹⁶ Sixty beams of

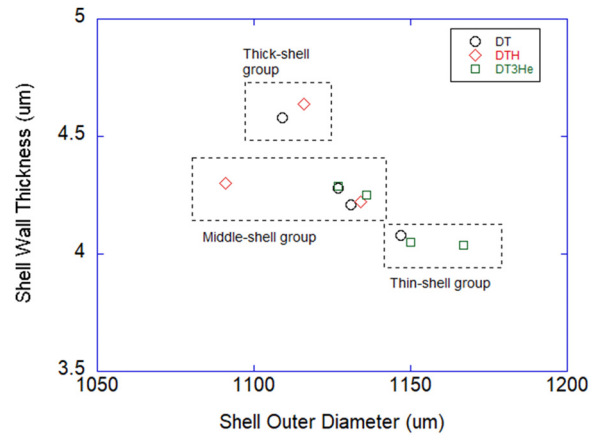


FIG. 1. Outer diameter and wall thickness of 11 capsules.

TABLE I. As-shot conditions for 11 capsules.

Shot#	Type	D ₂ (atm)	T ₂ (atm)	H ₂ (atm)	³ He (atm)	Shell material	Wall thickness (um)	O.D. (um)
Middle-shell group								
77977	DT	8.83	0.48	0	0	SiO ₂	4.28	1127
77980	DT	8.82	0.48	0	0	SiO ₂	4.21	1131
77976	DTH	0.57	4.62	4.11	0	SiO ₂	4.30	1091
77981	DTH	0.57	4.62	4.11	0	SiO ₂	4.22	1134
77978	DT ³ He	3.55	0.49	0	7.54	SiO ₂	4.29	1127
77979	DT ³ He	3.54	0.49	0	7.54	SiO ₂	4.25	1136
Thick-shell group								
77973	DT	8.89	0.48	0	0	SiO ₂	4.58	1109
77975	DTH	0.57	4.65	4.14	0	SiO ₂	4.64	1116
Thin-shell group								
77984	DT	8.81	0.48	0	0	SiO ₂	4.08	1147
77985	DT ³ He	3.54	0.49	0	6.33	SiO ₂	4.05	1150
77986	DT ³ He	3.53	0.49	0	7.1	SiO ₂	4.04	1167

351 nm UV light were focused on a spherical target in a 1-ns square pulse. The total energy delivered to capsules was 26–27 kJ, with smoothing by spectral dispersion and with SG5 phase plates. There was good agreement between requested and delivered laser pulse shape and power. When a total of 27 kJ was requested, an average of 26.1 kJ was delivered during the shot day. The standard deviation of laser energy was only 170 J (0.65% variation). For 10 out of 11 shots, the beam-to-beam energy imbalance was low between 2.5% and 2.8% rms. However, during shot number 77976 (DTH, middle-thickness-shell), one beam was lost and a 11.8% imbalance was obtained.

The principle parameter diagnosed was the DT neutron yields [$D + T \rightarrow {}^4\text{He} + n$ (14.1 MeV)] measured from a copper activation and a neutron time-of-flight (nTOF) suite (15.8 m nTOF, 12 m nTOF, 5.4 m nTOF, and 8×4 nTOF). The nTOF detectors also measured the DT-burn averaged ion temperature, which was determined from the Doppler broadening of the neutron signal. In addition to DT neutron yields, an 8×4 nTOF detector was fielded to measure DD and/or TT neutron yields simultaneously. Higher D concentrations of the 95/5 DT capsule and the DT³He (D/T = 14/1) allowed for both DT and DD yield measurements. However, for the DTH capsule, the DD neutron signal was too low to be detected and the TT neutron signal faced interference from the large background of the DT neutron signal. Temporal diagnostics of the fusion yield include the neutron temporal diagnostic (NTD) for measuring DT-n burn history and the gas Cherenkov detector (GCD) for measuring the DT gamma-ray branch [$D + T \rightarrow {}^5\text{He} + \gamma$ (16.75 MeV)].

In addition to anomalous yield reduction previously reported in Refs. 1–3, there were observations of larger imploded core image size in implosions with fuel mixtures. In the previous DT³He mixture implosion,³ the image size was ~25% larger than simulation. A similar trend was seen when argon was added to the D₂ fuel as a tracer.¹ These observations (larger image size than expected or less compression than expected) are qualitatively consistent with the observed anomalous yield reduction. However, as the previous x-ray image observations^{1,2} were made for the non-hydro-equivalent capsules, it

was not straightforward to compare x-ray image sizes as a function of fuel mixtures. In this paper, x-ray imaging from a time-integrated/energy-resolved GMXI (gated monochromatic x-ray imager¹⁷) was used for three hydro-equivalent fuel types.

Based on the burn-averaged areal density (ρR) measurement, Rygg *et al.* suggested that 50/50 D³He might experience less compression, resulting in a lower yield.² To confirm whether such reduced compression would be observed in DT³He and/or DTH, we fielded two diagnostic techniques available at the Omega laser facility. First, using a charged particle spectrometer (CPS),¹⁸ fuel ρR was inferred from the knock-on proton yield [$n(14.1 \text{ MeV}) + p \rightarrow n' + p^* (<14.1 \text{ MeV})$] on the DTH capsules, and from the knock-on deuteron yield [$n(14.1 \text{ MeV}) + D \rightarrow n' + D^* (<12.5 \text{ MeV})$] on the 95/5 DT capsules. Second, a diagnostics for areal density (DAD)—gamma-ray based shell ρR detector—was used for three DT, DTH, and DT³He capsules.¹⁹ The DAD is a glass Cherenkov detector, which yields a 0.3 MeV gamma-ray energy threshold for producing Cherenkov photons. The DAD was cross-calibrated against CPS at the previous glass shell implosion experiment.

IV. EXPERIMENTAL RESULTS

A. Observables supporting hydrodynamic equivalent implosions of DT, DTH, and DT³He

The implosion observables from the three capsule types (DT, DTH, and DT³He) are compared with each other to examine if imploding capsules behave equivalently in a hydrodynamic way. Five observables were used: neutron bang time, ion temperature, x-ray self-emission, and areal density of fuel or ablator. Figure 2(a) shows the time of peak neutron emission (bang time) obtained from the NTD, as a function of shell thickness and a fuel fill type. As the shell thickness increased from 4.0 μm to 4.6 μm , neutron bang time increased linearly from 1200 ps up to 1325 ps. One DTH capsule with a 4.3 μm wall thickness (#77976) showed an earlier bang time by 40 ps than other capsules with a similar wall thickness. As shown in Table I, the 77976 DTH capsule had a smallest diameter (i.e., 1091 μm), resulting in a

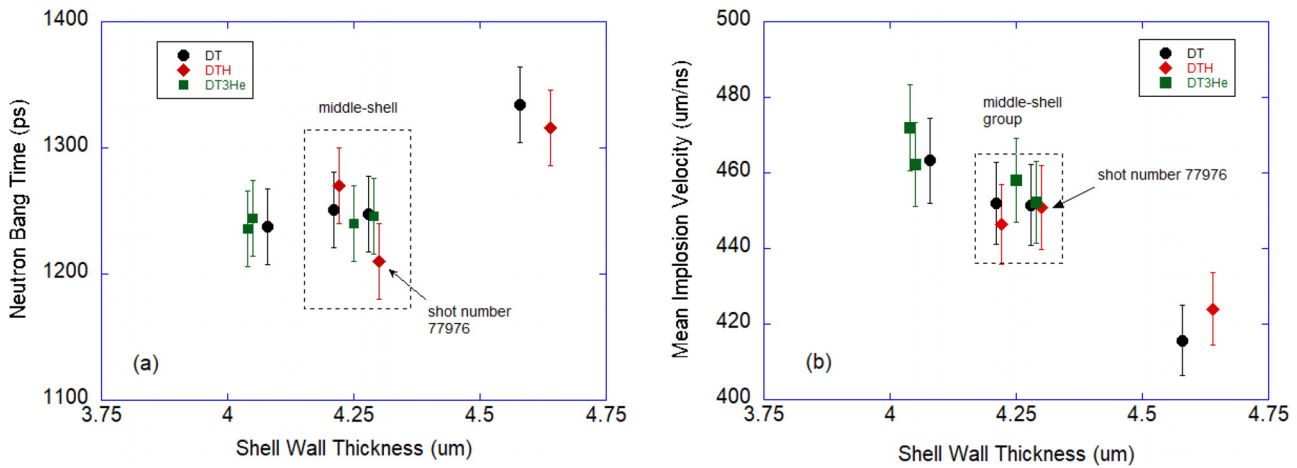


FIG. 2. (a) Observed DT bang time as a function of shell thickness and fuel fill type; (b) mean implosion velocities are consistent with each other between DTH, DT, and DT³He within each shell group, suggesting three types of implosions are equivalent in a hydrodynamic way.

shortest distance to travel than others. We calculated a mean implosion velocity (i.e., radius/bangtime) and plotted it as a function of shell-wall thickness [Fig. 2(b)]. The mean implosion velocity of #77976 is similar to other mid-shell capsules, suggesting its hydrodynamic-equivalent behavior with others. As shell thickness increases, the mean implosion velocity decreases, irrespective of the fuel fill type.

Figure 3 shows time-integrated, burn-averaged DT ion temperature (T_i) measured from the 15.8 m nTOF as a function of shell thickness and fill type. As the wall thickness of the glass shell increases, T_i decreases linearly from 9 to 6 keV. There does not appear to be a strong temperature dependence on the fill type, within the error bars. T_i is strongly affected by implosion velocity; therefore, it can be inferred that implosions from the three fill types behave similarly within the same shell group (i.e., wall thickness and diameter). In Fig. 3, error bars of T_i are 0.5 keV, which is a total uncertainty in T_i

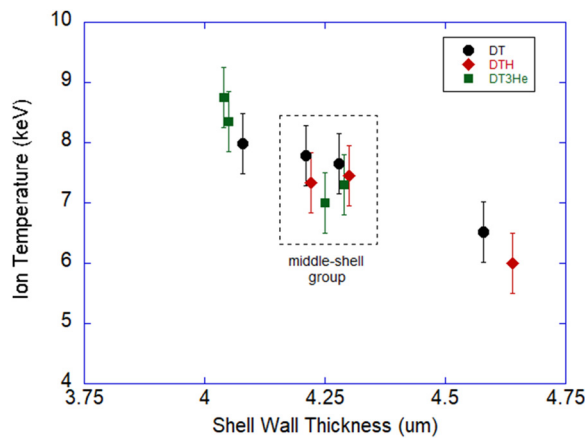
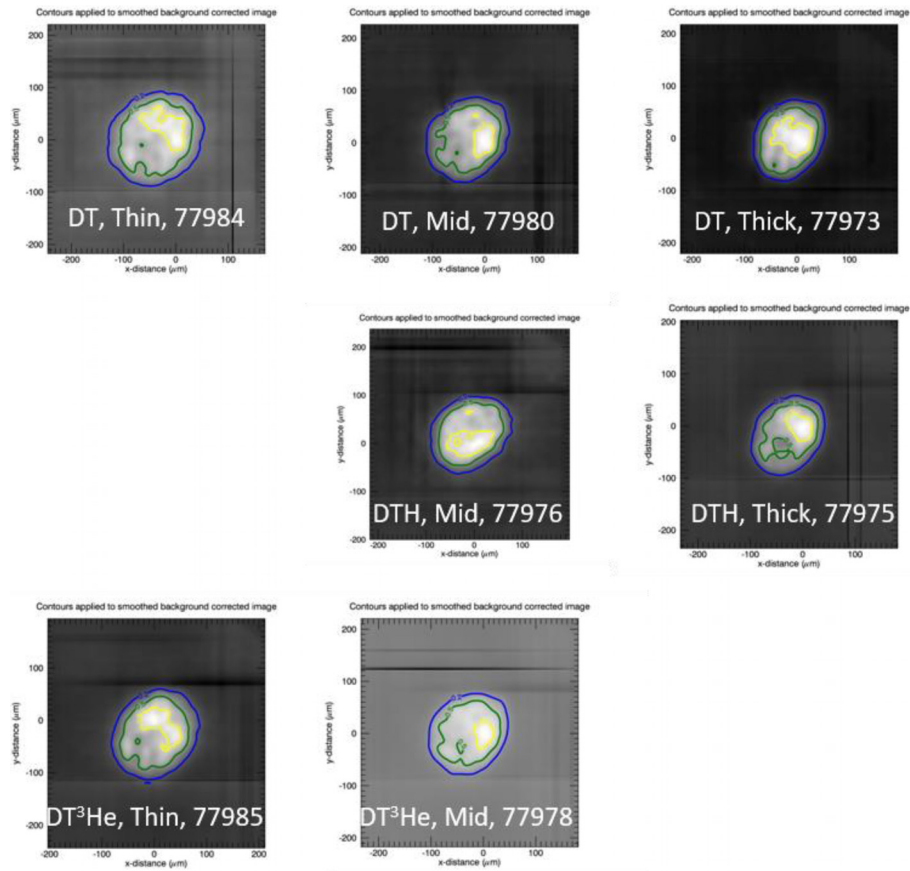


FIG. 3. Ion temperature are consistent with each other between DTH, DT, and DT³He within each shell group, suggesting three types of implosions are equivalent in a hydrodynamic way.

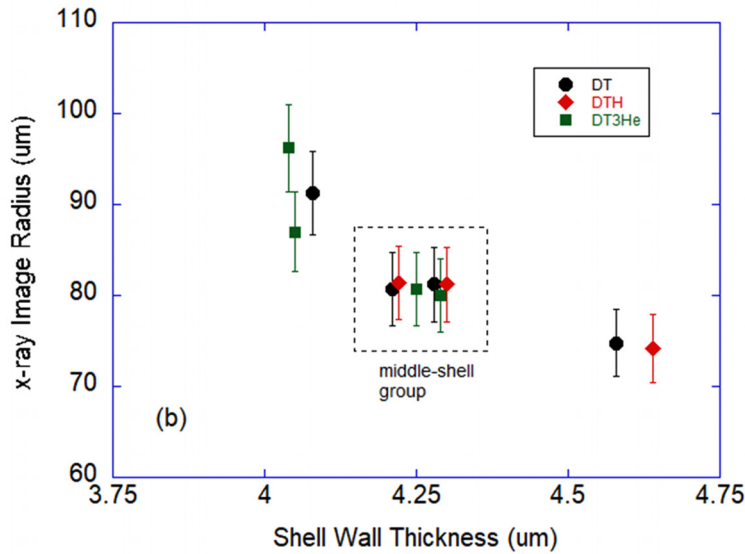
measurement contributed by both a systematic uncertainty and a statistical uncertainty. For a later yield ratio analysis to be shown in Secs. IV B and IV C, only statistical uncertainty in T_i will be used because the systematic uncertainty is canceled out for the ratio of DTH/DT and DT³He/DT analysis. To get a statistical shot-to-shot uncertainty in T_i , we calculated the ratio of two detector signals (15.8 m nTOF/12 m TOF) for 11 shots. The random shot-to-shot uncertainty of 15.8 m nTOF and 12 m nTOF is much smaller. The standard deviation in T_i ratio was 2.7% during DTH shots, 1.8% in DT shots, and 3.2% in DT³He shots. Appendix B describes how the statistical uncertainty in T_i was determined.

Figure 4(a) shows seven images taken by a GMXI x-ray camera. The first row contains three DT shots, the second row contains two DTH shots, and third row contains two DT³He shots. The first column is from a thin-shell group, second column from a middle-shell, and the last column from a thick-shell group. On top of each image, three contours lines are displayed; 20% contour in blue, 50% contour in green, and 80% contour in yellow. Within each shell group (i.e., thin-, middle-, thick-shell), the average radius and shape of the implosion images were consistent with each other between DT, DTH, and DT³He.

Figure 4(b) shows the x-ray image radius measured from fuel-core self-emission, as a function of shell thickness and fill type. The first step in calculating the image radius was to subtract a background image (acquired before the shot) from the foreground image. Any noise signatures visible in this image were removed by zeroing negative pixel values. High intensity pixel values caused by neutron interactions were also set to zero. The image was then convolved with a Gaussian-shaped smoothing kernel, with a width equal to two pixels (5.6 μm at the target plane). The next step was to correct the magnification of horizontal- and vertical-direction. The background under the core emission was estimated by applying a third-order polynomial fit. The average radius of the contour points was calculated relative to the center of the image, defined as the center of mass of the intensity within the 20% contour. The standard deviation of the radius was based on the radii at fixed intervals around the contours. As shell thickness increases, the x-ray image radius decreases from ~95 μm



(a)



(b)

FIG. 4. (a) Implosion images taken by GMXI x-ray camera. On top of each images, three contours lines are shown; 20% contour in blue, 50% contour in green, and 80% contour in yellow. Each image radius was measured by using 20% contour. Implosion images are consistent with each other between DTH, DT, and DT³He within each shell group, suggesting three types of implosions are equivalent in a hydrodynamic way. (b) Observed x-ray image radius of DTH, DT, and DT³He are consistent with each other within each shell group, suggesting three types of implosions are equivalent in a hydrodynamic way.

(convergence ratio ~ 6) to $75\ \mu\text{m}$ (convergence ratio ~ 7), indicating that a thicker shell compresses fuel more in the $4\text{--}4.6\ \mu\text{m}$ range. At a given shell thickness group, however, similar x-ray image size was achieved, irrespective of the fuel fill type. For example, the middle-thickness shell group produced $76\text{--}81\ \mu\text{m}$ image size in radius for all three fill types. It appears that the DT, DT³He, and DTH capsules compressed fuel similarly.

An alternative approach to monitor hydrodynamic compressibility during the implosion is to measure the areal density (ρR) of the shell or fuel. Figure 5(a) shows fuel ρR of the 95/5 DT capsules inferred from the knock-on deuteron yield [$n(14.1\ \text{MeV}) + \text{D} \rightarrow \text{n}' + \text{D}^* (<12.5\ \text{MeV})$], as well as fuel ρR of the DTH capsules inferred from the knock-on proton yield [$n(14.1\ \text{MeV}) + \text{p} \rightarrow \text{n}' + \text{p}^* (<14.1\ \text{MeV})$], measured by a CPS. The fuel ρR increases slightly as shell thickness increases (more compression), but no significant distinction between the DT and DTH fill type is observed within experimental error bars. Low yield from DT³He implosions prevented us from extracting fuel ρR for the DT³He case. For measuring shell ρR , a DAD was used to monitor the shot-to-shot variation of the gamma-ray emission produced when the DT fusion neutrons pass through an imploding glass shell [i.e., $n(14.1\ \text{MeV}) + \text{SiO}_2 \rightarrow \text{SiO}_2(\text{n}, \text{n}'\gamma)$].

Figure 5(b) shows the glass shell ρR in units of mg/cm^2 as a function of shell thickness. The glass shell ρR increases from ~ 4 to $\sim 10\ \text{mg}/\text{cm}^2$ as the shell thickness increases from 4.1 to $4.6\ \mu\text{m}$. However, there was no apparent dependency on shell ρR with fuel fill type.

The inferred radii from the observed fuel ρR appear consistent with the x-ray emission radius r_{xray} shown in Fig. 4(b). Using the measured fuel ρR , we calculated the corresponding radius, using the simple relation $\rho R_{\text{fuel}} = (\text{mass}/\text{volume})R$. Here, we use the initial fuel mass, obtained from the initial pressures assuming the pressures are quoted at room temperature and using the ideal gas law. For volume, we take $(4\pi R^3)/3$, which means $R_{\text{inferred}} = \sqrt{\frac{3\text{mass}}{4\pi(\rho R_{\text{fuel}})}}$. We inferred the radii in Fig. 5(c), which appear consistent with, although not identical to the x-ray image radii shown in Fig. 4(b).

B. Increased DT yield over prediction due to H addition

Five neutron yield detectors were placed at different locations and recorded DT neutron yields for each capsule implosion. The final DT neutron yield was determined by averaging the values from the five detectors by weighting their errors. Figure 6(a) shows the final DT neutron yield as a function of shell thickness and fuel fill type.

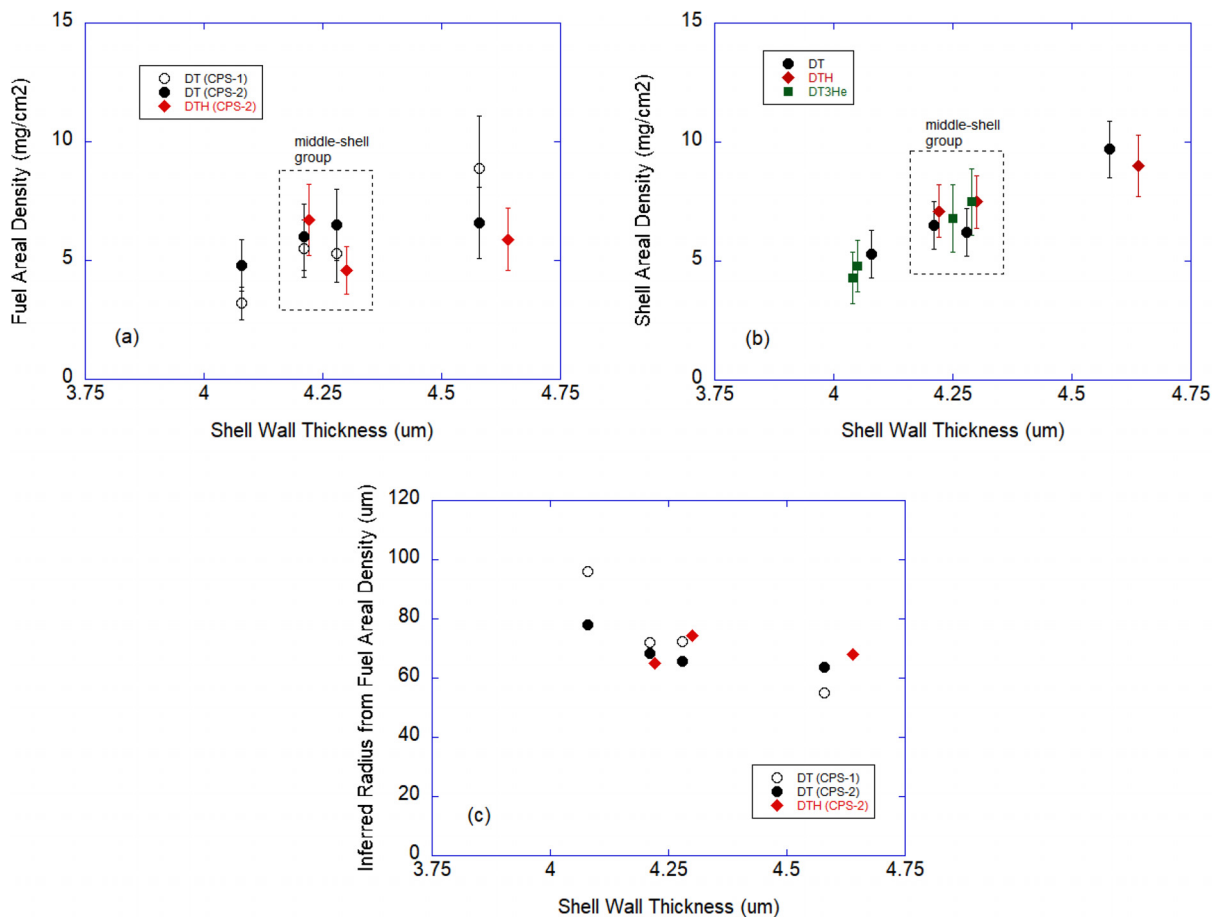


FIG. 5. (a) Fuel areal densities of DTH are consistent with that of DT within error bars, (b) shell areal densities of DTH, DT, and DT³He are consistent with each other, supporting the conclusion that three types of implosions are equivalent in a hydrodynamic way, (c) radius inferred from fuel ρR measurement agrees with x-ray emissions.

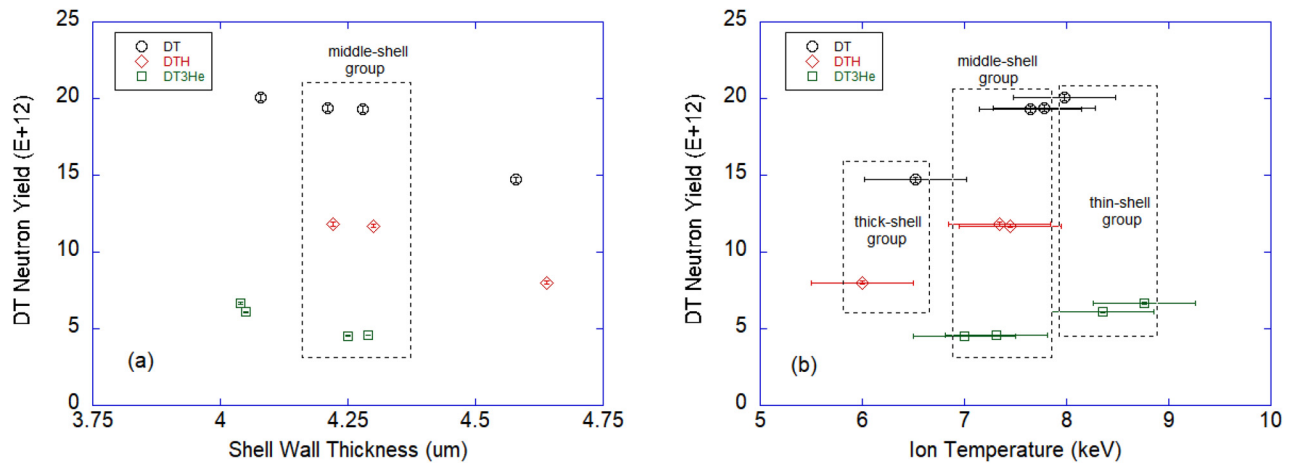


FIG. 6. (a) Observed DT yield as a function of shell thickness; (b) observed DT yields from three types of fuel as a function of ion temperature.

The 95/5 DT capsules produced the most neutron yield in the range of $(15\text{--}20) \times 10^{12}$. As the capsule was switched to DTH, the neutron yield dropped to $(7\text{--}12) \times 10^{12}$. Finally, the DT^3He capsules produced the least yield in the range of $(4\text{--}6) \times 10^{12}$. When the shell conditions and fuel fill are similar, the neutron yield became quite reproducible within a 3% shot-to-shot variation (e.g., 2 DT^3He shots at thin-shell group, 2 DT shots at middle-shell group, 2 DTH shots at middle-shell group, and 2 DT^3He shots at middle-shell group). Figure 6(b) is another way to plot the observed yield as a function of ion temperature by combining Figs. 6(a) and 3. For all three types of fill, DT neutron yields were increased as ion temperature increased. The yield to ion temperature slope of 95/5 DT and that of DTH are similar, but the slope of DT^3He is less steep in comparison.

In Table II, the performance of DTH implosions was compared against 95/5 DT control capsules. Table II includes experimental observables such as DT neutron yield (column C), ion temperature (column D), x-ray image radius (column E), and burn duration (column F). Using these data, we then conducted analysis for the expected yield ratio, $(Y_{DT}^{DTH}/Y_{DT}^{DT})_{\text{expected}}$, which can be seen in columns G through J. Scaling corrections help to compensate for small departures from hydrodynamic equivalence by replacing the integrals in Eqs. (3), (5), and (8) with the product of time averages of the various terms in the integrand. This approximation assumes sufficiently similar time and space behavior of all the terms. As a first step, $(Y_{DT}^{DTH}/Y_{DT}^{DT})_{\text{expected}}$ shown in column G assumes identical ion temperatures, burn volumes, and burn durations between all implosions; therefore, the expected yield ratio is simplified as $(Y_{DT}^{DTH}/Y_{DT}^{DT})_{\text{expected}} \sim [f_D f_T (\rho/\bar{m})^2]^{DTH} / [f_D f_T (\rho/\bar{m})^2]^{DT}$, where the actual fill pressure and capsule size were used to calculate f_D , f_T , ρ , \bar{m} for each shot. For middle-shell group, an average of two DT shots (#77977, #77980) was used and #77973 DT shot was used for thick-shell group, respectively. Column H refines column G by including actual ion temperatures measured, which affect the DT fusion reactivity term; $(Y_{DT}^{DTH}/Y_{DT}^{DT})_{\text{expected}} \sim [f_D f_T (\rho/\bar{m})^2 \langle \sigma v(T_i) \rangle]^{DTH} / [f_D f_T (\rho/\bar{m})^2 \langle \sigma v(T_i) \rangle]^{DT}$.

Additionally, column I includes actual burn volumes (assuming the burn radius is proportional to the x-ray image radius $r_{x\text{-ray}}$): $(Y_{DT}^{DTH}/Y_{DT}^{DT})_{\text{expected}} \sim [f_D f_T (\rho/\bar{m})^2 \langle \sigma v(T_i) \rangle r_{x\text{-ray}}^3]^{DTH} / [f_D f_T (\rho/\bar{m})^2 \langle \sigma v(T_i) \rangle r_{x\text{-ray}}^3]^{DT}$, and column J includes burn duration τ_{burn} : $(Y_{DT}^{DTH}/Y_{DT}^{DT})_{\text{expected}} \sim [f_D f_T (\rho/\bar{m})^2 \langle \sigma v(T_i) \rangle r_{x\text{-ray}}^3 \tau_{\text{burn}}]^{DTH} / [f_D f_T (\rho/\bar{m})^2 \langle \sigma v(T_i) \rangle r_{x\text{-ray}}^3 \tau_{\text{burn}}]^{DT}$. As a result, final $(Y_{DT}^{DTH}/Y_{DT}^{DT})_{\text{expected}}$ is 0.51–0.52 in the middle-shell group and 0.47 in the thick-shell group. Column K shows the observed yield ratio $(Y_{DT}^{DTH}/Y_{DT}^{DT})_{\text{observed}}$, which is 0.60–0.61 in the middle-shell group and 0.55 in the thick-shell group. Finally, column L shows the ratio of column K against J, $[(Y_{DT}^{DTH}/Y_{DT}^{DT})_{\text{observed}}] / [(Y_{DT}^{DTH}/Y_{DT}^{DT})_{\text{expected}}]$. The three DTH capsules show a factor of $1.17 \pm 12.8\%$ or 1.17 ± 0.15 yield increase compared against DT in average, supporting inverse Rygg effect due to H-addition. Appendix B gives a description of how the fractional uncertainties in column G through L were calculated.

C. Decreased DT yield over prediction due to ^3He addition

Table III shows the performance of DT^3He implosions compared against 95/5 DT control capsules. Following the analysis steps shown in Sec. IV B, we can anticipate $(Y_{DT}^{\text{DT}^3\text{He}}/Y_{DT}^{DT})_{\text{expected}}$ of 0.33–0.37 for middle-shell group and 0.43–0.62 for thin-shell group (shown in column J), but the experimental yield ratios $(Y_{DT}^{\text{DT}^3\text{He}}/Y_{DT}^{DT})_{\text{observed}}$ are 0.23–0.24 for the middle-shell group and 0.30–0.33 for the thin-shell group. Column L shows the ratio of column K against J, $(Y_{DT}^{\text{DT}^3\text{He}}/Y_{DT}^{DT})_{\text{observed}} / [(Y_{DT}^{\text{DT}^3\text{He}}/Y_{DT}^{DT})_{\text{expected}}]$. The four DT^3He capsules show a factor of 0.65 ± 0.13 yield reduction in average, supporting Rygg-effect due to ^3He -addition. Appendix B gives a description of how the fractional uncertainties in column G through L were calculated.

Figure 7 summarizes the $(Y_{DT}^{DTH}/Y_{DT}^{DT})_{\text{observed}} / (Y_{DT}^{DTH}/Y_{DT}^{DT})_{\text{expected}}$ and $(Y_{DT}^{\text{DT}^3\text{He}}/Y_{DT}^{DT})_{\text{observed}} / (Y_{DT}^{\text{DT}^3\text{He}}/Y_{DT}^{DT})_{\text{expected}}$ shown in column L of

TABLE II. Experimental observables for DTH and DT capsules.

A	B	C	D	E	F	G	H	I	J	K	L
Shot#	Type	DT neutron yield (measured)	Ion temperature (keV)	x-ray image radius (μm)	Burn duration (ps)	Expected yield ratio (as shot, composition and mass density correction)	Expected yield ratio (after correcting reactivity)	Expected yield ratio (after correcting reactivity, burn volume)	Expected yield ratio (after correcting reactivity, burn volume, burn duration)	Observed yield ratio (DTH/DT)	Observed/expected yield ratio (column K/column J)
Middle-shell group											
77976	DTH	1.17×10^{13}	7.45	81.2	109	$0.61 \pm 2.2\%$	$0.55 \pm 9.2\%$	$0.56 \pm 11.2\%$	$0.51 \pm 12.1\%$	$0.60 \pm 1.3\%$	$1.18 \pm 12.2\%$
77981	DTH	1.18×10^{13}	7.34	81.4	113	$0.62 \pm 2.2\%$	$0.54 \pm 9.2\%$	$0.55 \pm 11.2\%$	$0.52 \pm 12.1\%$	$0.61 \pm 1.3\%$	$1.18 \pm 12.2\%$
77977	DT	1.93×10^{13}	7.65	81.2	119
77980	DT	1.94×10^{13}	7.78	80.7	119
Thick-shell group											
77975	DTH	8.02×10^{12}	6.0	74.2	123	$0.63 \pm 2.4\%$	$0.48 \pm 10.8\%$	$0.47 \pm 12.7\%$	$0.47 \pm 14.0\%$	$0.55 \pm 1.5\%$	$1.15 \pm 14.1\%$
77973	DT	1.47×10^{13}	6.52	74.8	122

TABLE III. Experimental observables for DT³He and DT capsules.

A	B	C	D	E	F	G	H	I	J	K	L
Shot#	Type	DT neutron yield (measured)	Ion temperature (keV)	x-ray image radius (μm)	Burn duration (ps)	Expected yield ratio (as shot, composition term only)	Expected yield ratio (after correcting reactivity)	Expected yield ratio (after correcting reactivity, burn volume)	Expected yield ratio (after correcting reactivity, burn volume, burn duration)	Observed yield ratio (DT ³ He/DT)	Observed/expected yield ratio (column K/column J)
Middle-shell group											
77978	DT ³ He	4.57×10^{12}	7.31	80.0	130	$0.41 \pm 14.4\%$	$0.35 \pm 17.8\%$	$0.34 \pm 18.4\%$	$0.37 \pm 20.7\%$	$0.24 \pm 1.3\%$	$0.64 \pm 20.7\%$
77979	DT ³ He	4.54×10^{12}	7.0	80.7	129	$0.41 \pm 14.4\%$	$0.30 \pm 17.9\%$	$0.30 \pm 18.5\%$	$0.33 \pm 20.8\%$	$0.23 \pm 1.3\%$	$0.72 \pm 20.8\%$
77977	DT	1.93×10^{13}	7.65	81.2	119
77980	DT	1.94×10^{13}	7.78	80.7	119
Thin-shell group											
77985	DT ³ He	6.09×10^{12}	8.35	87.0	120	$0.41 \pm 14.5\%$	$0.47 \pm 17.8\%$	$0.41 \pm 18.0\%$	$0.43 \pm 21.2\%$	$0.30 \pm 1.3\%$	$0.70 \pm 21.3\%$
77986	DT ³ He	6.67×10^{12}	8.76	96.2	112	$0.41 \pm 14.5\%$	$0.54 \pm 17.7\%$	$0.63 \pm 17.9\%$	$0.62 \pm 21.2\%$	$0.33 \pm 1.3\%$	$0.53 \pm 21.2\%$
77984	DT	2.01×10^{13}	7.98	91.3	113

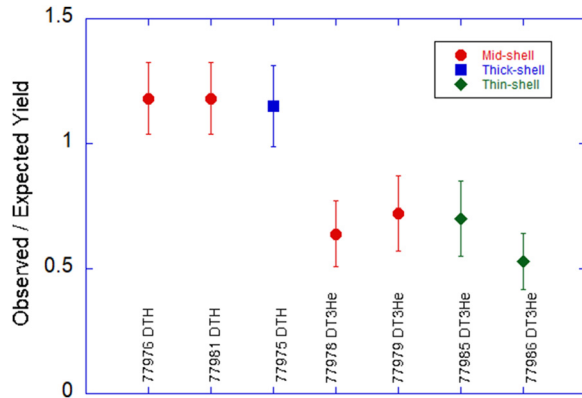


FIG. 7. Observed yield against analytic yield formula shows that experimental DTH capsules produced a factor of 1.17 ± 0.15 times more yield and experimental DT³He capsules produced a factor of 0.65 ± 0.13 times less yield.

Tables II and III, respectively. The observed neutron yields from DTH capsules are consistently higher than the estimated DT neutron yield by an average of 1.17 ± 0.15 , supporting the inverse Rygg effect due to the addition of H. The observed yields from the DT³He capsules were a factor of 0.65 ± 0.13 lower than the estimated neutron yield. The present yield reduction with a factor of 0.65 is not as strong as the previous results,² which were approximately a 0.5 reduction factor. Rygg *et al.*² used smaller radius shells ($\sim 435 \mu\text{m}$ in radius) and achieved a longer bang time (~ 1.8 ns). Therefore, the mean implosion velocity during the Rygg *et al.* experiment was on the order of $240 \mu\text{m/ns}$, much slower than this experiment ($410\text{--}470 \mu\text{m/ns}$). During an implosion with a high mean velocity (like this experiment), inter-species ion diffusion may not have enough time to fully develop; therefore, the yield reduction factor can be small. One of the results that Rygg *et al.* presented in 2006 publication (Fig. 6 in Ref. 2) is that as shell thickness is thinner, the Rygg effect (or \tilde{Y}_{ratio} in Ref. 2) is decreased for both 3 and 15 atm conditions. It is known that a thin-shell implosion tends to produce a higher implosion velocity;²⁰ therefore, the reduced Rygg-effect (or small \tilde{Y}_{ratio}) seen at thin-shell data can be correlated with a high mean velocity. Therefore, a smaller Rygg-effect (0.64 rather than 0.5) observed in our experiment (i.e., high mean implosion velocity) remains somewhat consistent with the original 2006 Rygg *et al.* result.

D. Measured DD/DT yield ratio in DT³He capsule supporting ion separation

As shown in Casey *et al.*,¹⁵ neutron yield ratio (e.g., DD/DT or TT/DT) is a useful diagnostic signature because the yield ratio depends weakly on the shot-to-shot variation, whereas absolute yield method (e.g., DD yield in D³He capsule or DT yield in DT³He capsule) requires a control shot to compare (e.g., DD capsule as a control shot for D³He capsule or DT capsule as a control shot for DT³He capsule). To test whether the yield reduction (a factor 0.65 ± 0.13) observed from the present DT³He implosion was caused by the depletion of D in the core, we measured both the DD and DT neutron yields. The measured Y_{DD}/Y_{DT} ratio (open square) was plotted in Fig. 8 as a function of T_i . The dashed line shown in Fig. 8 is the calculated

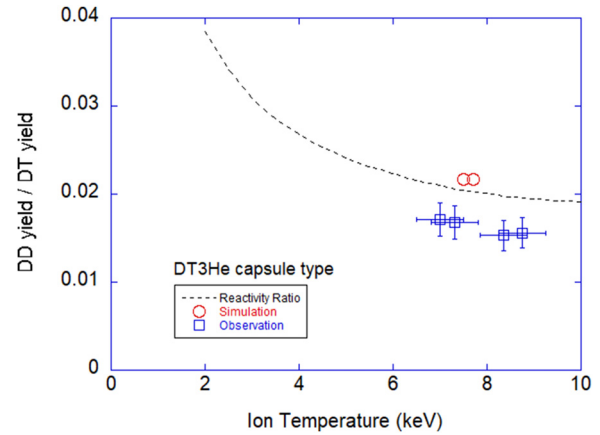


FIG. 8. Measured DD/DT yield using a DT³He capsule (open square) was lower than expected (open circle or dashed line).

Y_{DD}/Y_{DT} obtained from fusion reactivity scaling [i.e., $(Y_{DD}/Y_{DT})^{DT^3He} = (f_D \langle \sigma v \rangle_{DD})^{DT^3He} / (2f_T \langle \sigma v \rangle_{DT})^{DT^3He}$] as a function of T_i . Open circles show 1D simulation results obtained from xRAGE,²¹ which agrees with the reactivity scaling (dashed line). Over the measured range of T_i (7–9 keV), the observed DD/DT yield was $\sim 80\%$ of the expected DD/DT yield ratio either from the reactivity scaling or numerical simulation. The discrepancy between the observed yield ratio (DD/DT) and the expected yield ratio can be explained by the lower D concentration in the core, similarly observed by Casey *et al.* from the 50/50 DT capsule.¹⁵ For the DTH implosions, we attempted to measure TT neutron yield to test whether the observed TT/DT yield ratio would be higher than the simulated one. However, the TT neutron yield could not be measured because of interference from the large background from the DT neutron yield. It appears that an initial 5% D concentration in the present DTH capsules still produces too much background signal for the TT neutron signatures. Future DTH experiments using a reduced D initial concentration (e.g., $< 5\%$ D) will be needed to achieve the TT/DT yield measurement and further qualify the inverse Rygg effect in the DTH capsule.

V. ANALYSIS OF DTH AND DT³He CAPSULES USING SIMULATION-BASED BAYESIAN INFERENCE

If the capsules are not hydrodynamically equivalent, the simple analysis described above is not strictly valid because the integrals in Eqs. (3), (5), and (8) are not equal. Scaling corrections, as described in the discussion of Tables II and III, help to compensate for small departures from hydrodynamic equivalence, by replacing the integrals in Eqs. (3), (5), and (8) with the product of time averages of the various terms in the integrand. This approximation assumes sufficiently similar time and space behavior of all the terms. But to be most widely applicable, a more general analysis technique is required, based on numerical simulations accounting for processes which might negate hydrodynamic equivalence, such as radiation transport, heat conduction, departures from ideal-gas equation-of-state (EOS), and uncontrolled variations in fuel compositions (hydrodynamic mix, which ought to behave similarly in hydrodynamically equivalent capsules, is not such a process). The general technique we employ uses

simulation-based Bayesian inference and is valid whether or not the capsules are hydrodynamically equivalent.

We have presented evidence that the capsules in this experiment were indeed nearly hydrodynamically equivalent and described how to make small scaling corrections to correct for departures. Nevertheless, this experiment affords us a good opportunity to exercise the general simulation-based technique. Essentially, we use numerical simulations, constrained by the data, to make “predictions” (in quotes, because the experiments have already been conducted) of the behavior of the DTH and DT³He capsules, together with uncertainty bounds, based on observations of the DT capsules. If the DTH and DT³He capsules’ behavior departs significantly from predictions, allowing for uncertainty, then we might conclude we have evidence for an incorrect model of effects such as species separation. It is easy, of course, to run a few simulations that disagree with data; one can conclude very little from such an exercise. It is more meaningful to show that a numerical model does explain a significant set of observations, and yet is unable to account for a novel type of experiment. That is the approach we follow here.

To carry out this analysis, we use the GPM/SA (Gaussian process models for simulation analysis) code.²² GPM/SA reads the results (“output”) from a large ensemble of 1D radiation-hydrodynamic numerical simulations of the analyzed capsules, spanning a volume of model-parameter input space; we regard the rad-hydro simulator as a mapping from the input space of model parameters to the output space of observed quantities of interest. GPM/SA then fits a Gaussian-process “emulator” to the simulator outputs, to allow rapid estimates of simulator outputs over all of input space, and samples the emulator using Markov chain Monte Carlo (MCMC) to infer the joint probability distribution of the input parameters giving a plausible fit of the outputs to observed capsule data. Using the symbol θ to represent the vector of input model parameters, we infer their joint probability distribution from Bayes’ Theorem

$$\mathbf{P}(\theta|y(x)) \propto \mathbf{P}(y(x)|\theta)\mathbf{P}(\theta) \quad (10)$$

given a vector of observable quantities y resulting from a set of experiments defined by experiment (or “geometry”) parameters x . Here $\mathbf{P}(y(x)|\theta)$ is the “likelihood” that observables y result from a simulation with model parameters θ and basically measures how well the simulation output $\mu(x, \theta)$ fits the data $y(x)$

$$\mathbf{P}(y(x)|\theta) \sim \exp \left\{ - \sum_i^{\text{caps}} \sum_j^{\text{obs}} \frac{[y_j(x_i) - \mu_j(x_i; \theta)]^2}{2\sigma_{ij}^2} \right\}, \quad (11)$$

where index i runs over capsules, index j runs over observables, and σ_{ij} is the uncertainty of observable j for capsule i . $\mathbf{P}(\theta)$ is the prior probability distribution of θ , which we take as just a flat distribution over a prescribed initial range. This expression describes the way the observations y constrain the allowed values of θ . Finally, GPM/SA can generate predictions, with uncertainty bounds, for capsules that are not part of the analysis set, based on the probability distribution of input parameters given by Eq. (10). For a “new” capsule, with experiment parameters x^* , the probability that an observable has the value y is

$$\mathbf{P}(y(x^*)|y(x)) = \int \mathbf{P}(y(x^*)|\theta)\mathbf{P}(\theta|y(x))d\theta \quad (12)$$

expressing how the probability distribution of θ limits the possible predicted observable values $y(x^*)$.

The value of simulation-based Bayesian inference, using large ensembles of simulations, results from several features. For one thing, it allows us to assign uncertainty bounds—“error bars”—to simulations and predictions, which is crucial when we are searching for small experimental effects. Historically, it has been very difficult to determine, from first principles, the uncertainty bounds on simulation results, so it was usually not done. Using statistical inference constrained by experimental data, however, it becomes feasible to quantify simulation uncertainty, as illustrated here. For another thing, this process enables model validation and hypothesis testing since they depend on uncertainty quantification to assess the significance of deviations between data and simulations. For a third thing, it was always a bit deceptive to present a single simulation as being the explanation for an experiment. Because the data are uncertain and the simulator is not perfect, it is likely that an infinity of other simulations, whether nearby or perhaps far away in input space, are equally plausible. By exploring input space, albeit with simplified, lower dimensional models, we gain better knowledge of the range of plausible calculational explanations of an experiment. Finally, because the simulation models are not perfect, it is conceptually more defensible, as a representation of our state of knowledge, to view their parameters as probability distributions rather than sharp values; that is what statistical inference provides.

A recent application of GPM/SA to the analysis of ICF capsules is described by Osthus *et al.*²³ who used the data from 22 “exposed” OMEGA capsule shots to calibrate a simulation model that was then used to “predict” the results (for laser absorbed fraction f_{abs} , DT yield Y_{DT} , DD yield Y_{DD} , and mean DT ion burn temperature T_{iDT}) for 16 other “hidden” shots that were significantly different (having thicker shells or different gas composition) than the exposed shots. Of 52 observed quantities for the 16 hidden capsules, 49 of the predictions (i.e., 94%) fell within the predicted 95% confidence interval, a satisfactory result.

The radiation-hydrodynamic simulator used in the present analysis is very similar to that used in Ref. 23 and identical to the simulator used by Zylstra *et al.*²⁴ in their observation and explanation of diffusion-dominated mixing in direct-drive ICF capsules. It is a 1D Lagrangian finite-difference radiation-hydrodynamics code, incorporating multigroup radiation diffusion, electron and ion thermal conduction, and geometric ray-tracing for laser propagation, refraction, and inverse-bremsstrahlung absorption. The full simulation model includes reduced laser intensity due to scattered light, artificial preheat of the capsule due to radiation or hot electrons, a buoyancy-drag model of hydrodynamic mix,²⁵ and the Zimmerman–Paquette–Kagan–Zhdanov (ZPKZ) ion-diffusion model.^{26–28} The ZPKZ ion-diffusion model incorporates thermodiffusion of multiple ion species, frictional ion heating, and the advective transport of ion enthalpy, in addition to the processes of concentration diffusion, barodiffusion,¹⁰ and electrodiffusion, which were the only processes included in an earlier version of the ion-diffusion model, as described in Ref. 11. There are no adjustable parameters associated with the ZPKZ model. The reduced laser intensity is characterized by a parameter f_{ls} , which is the fraction of incident laser energy that is introduced into the simulation. The preheat magnitude is set by a parameter f_{pre} , which is the fraction of incident laser energy that is distributed uniformly though the capsule at the beginning of the laser pulse. The hydrodynamic mix model

is governed by an initial turbulent scale length l . Thus, given a set of capsule geometry parameters \mathbf{x} , the simulator can be regarded as a mapping from a three-dimensional input space whose axes are the model parameters $\boldsymbol{\theta} = (f_{ls}, f_{pre}, l)$ to a multidimensional output space whose axes are the experimental observables $\mathbf{y} = (f_{abs}, Y_{DT}, T_{iDT}, \dots)$.

We analyzed all eleven shots listed in Table I. As shown in Table I, shots #77973, #77977, #77980, and #77984 were filled with DT, and had different shell thicknesses, representing the thick-, middle-, and thin-shell groups. These four shots constituted the calibration set, whose observed data $\mathbf{y}(\mathbf{x})$ we used to constrain the GPM/SA emulator. Then, using the emulator, we generated “predictions” $\mathbf{y}(\mathbf{x}^*)$ for the DTH- and DT³He-filled shots. As described below, we found that the emulator, when run without the ZPKZ ion-diffusion model, was able to explain the calibration set, but was unable to explain the behavior of the DTH and DT³He shots, providing evidence that some un-modeled effect associated with gas composition—perhaps species separation—was occurring. We also found that running the emulator with ZPKZ goes some way toward explaining the DTH and DT³He shots, again consistent with the hypothesis that species separation is occurring, although there are some remaining discrepancies. Because the discrepancies are small, careful attention to uncertainties is necessary, as we shall describe.

For each shot, we carried out simulations spanning a regular grid in input space. When using the ZPKZ ion-diffusion model, the grid

was defined by three values of the laser source fraction $f_{ls} \in [0.80, 0.90, 1.00]$, six values of the hydrodynamic-mix scale length $l \in [0, 0.02, 0.08, 0.15, 0.25, 0.40] \mu\text{m}$, and eight values of the preheat fraction $f_{pre} \in [0, 0.01, 0.015, 0.02, 0.025, 0.03, 0.05, 0.08]$. Thus, $3 \times 6 \times 8 = 144$ simulations were carried out for each shot when using ZPKZ. Without ZPKZ, the input-space grid was somewhat different because earlier work had showed that the likelihood would be optimized in a slightly different region of input space. Thus, without ZPKZ, the grid was defined by three values of $f_{ls} \in [0.70, 0.80, 0.90]$ and seven values of $l \in [0, 0.02, 0.08, 0.15, 0.25, 0.40, 0.60] \mu\text{m}$, with the same eight values of f_{pre} , so that $3 \times 7 \times 8 = 168$ simulations were carried out for each shot when not using ZPKZ. This means that a total of 312 simulations were done for each shot, counting both models, resulting in 3432 simulations over all eleven shots. Scanning a regular grid in this manner is not the most efficient way to sample a parameter space, specifically if it is high-dimensional, but for a 3D space it is feasible. Each simulation typically requires under 5 min of wall-clock time, on a single 36-core node of an Intel Xeon Broadwell cluster, with many simulations running simultaneously.

Figure 9 shows the projections of the joint probability distribution $\mathbf{P}(\boldsymbol{\theta} | \mathbf{y}(\mathbf{x}))$ for the input parameters $\boldsymbol{\theta} = (f_{ls}, f_{pre}, l)$ when the emulator was constrained by the five observables $\mathbf{y} = (Y_{DT}, T_{iDT}, f_{abs}, t_{bang}, \tau_{burn})$ for each of the four DT-filled shots #77973, #77977, #77980, and #77984, giving twenty observational

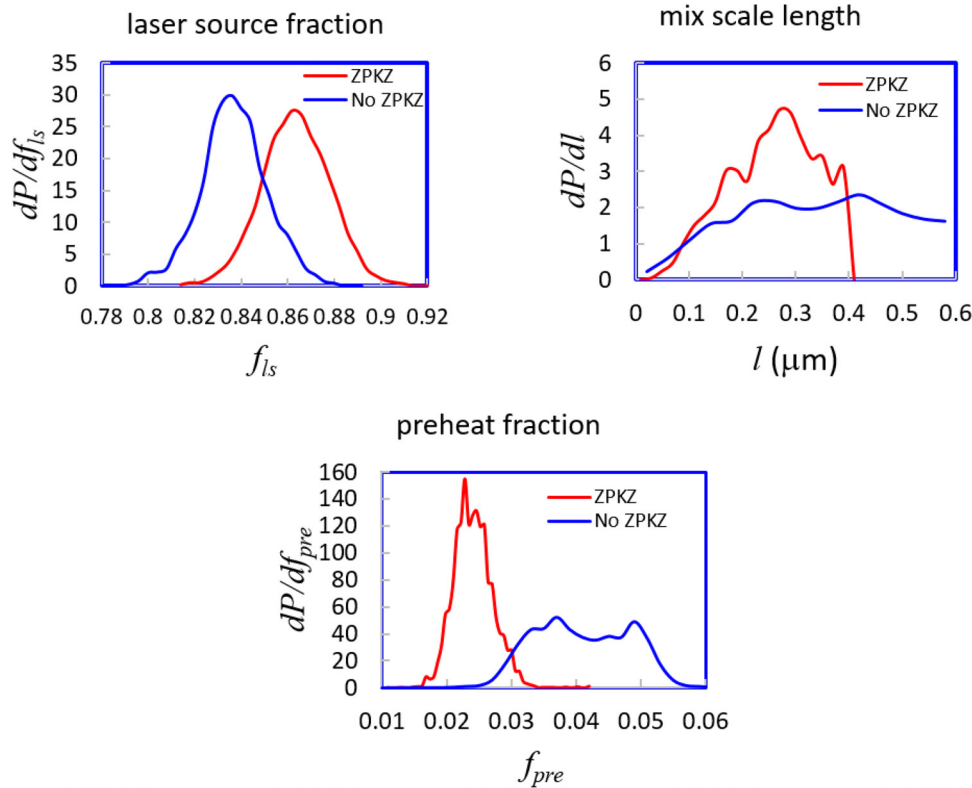


FIG. 9. Marginal distributions or projections of the joint probability distribution, for the input parameters f_{ls} , l and f_{pre} , when the emulator was constrained by the observed values of five quantities (Y_{DT} , T_{iDT} , f_{abs} , t_{bang} , τ_{burn}) for each of the four DT-filled shots #77973, #77977, #77980, and #77984. The integral of each curve is normalized to unity. The median and 95% confidence bounds of the distributions are $f_{ls} = 0.86 (\pm 0.03)$, $l = 0.27 (+0.13, -0.17) \mu\text{m}$, and $f_{pre} = 0.024 (+0.006, -0.005)$, with ZPKZ, and $f_{ls} = 0.84 (\pm 0.03)$, $l = 0.34 (+0.24, -0.28) \mu\text{m}$, and $f_{pre} = 0.041 (+0.013, -0.012)$, without ZPKZ.

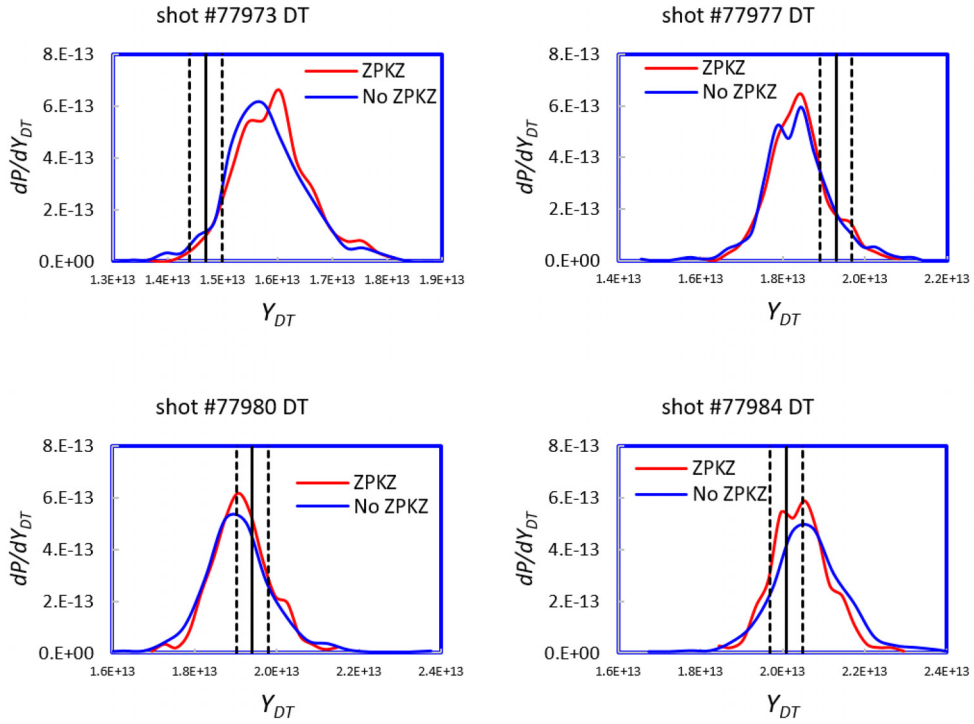


FIG. 10. Posterior distributions for DT yield for the four shots in the calibration set: #77973, #77977, #77980, and #77984. Vertical lines show the observed values of $Y_{DT} \pm 2\sigma_{obs}$, where $\sigma_{obs} = 1\%$. The medians of the posterior distributions agree with observations to better than $\sim 8\%$ for all four shots.

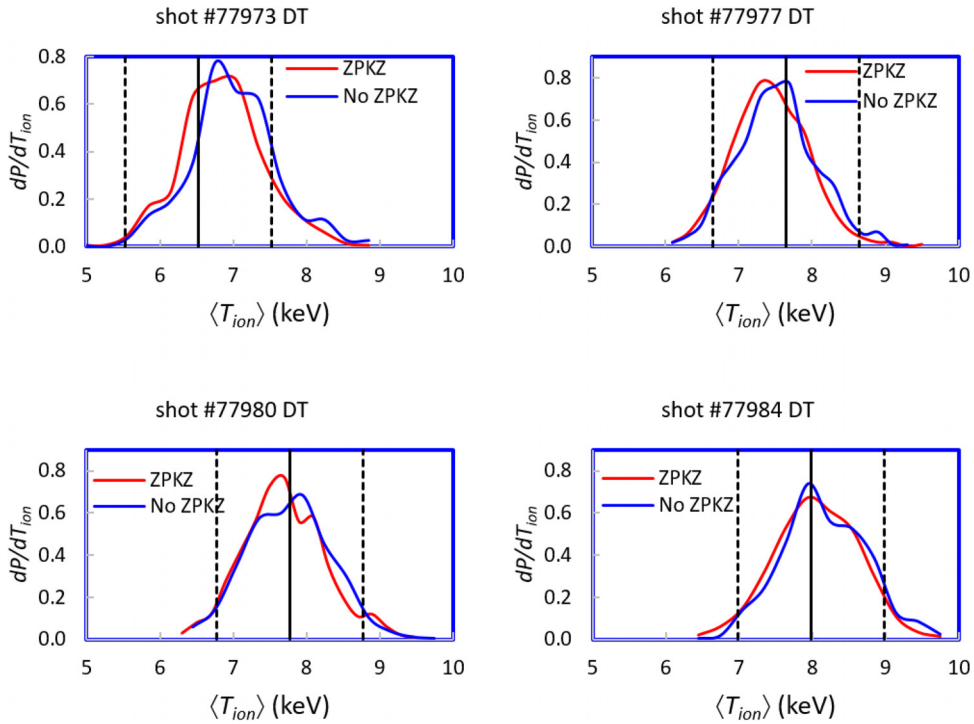


FIG. 11. Posterior distributions for average DT ion burn temperature for the four shots in the calibration set. Vertical lines show the observed values of $\langle T_i \rangle_{DT} \pm 2\sigma_{obs}$, where $\sigma_{obs} = 0.5$ keV. The median of the posterior distributions agree with observations to within $\sim 5\%$ and much better than $2\sigma_{pred}$ for all four shots.

constraints in all. The observational uncertainties σ_{obs} on Y_{DT} , T_{iDT} , f_{abs} , t_{bang} , τ_{burn} were assumed to be $\pm 1\%$, ± 0.5 keV, ± 0.05 , ± 0.05 ns, and ± 0.03 ns, respectively. Results are shown with and without the ZPKZ ion-diffusion model, when using about 20 000 MCMC samples.

Figure 10 shows the posterior probability distribution for DT yield for the four shots in the calibration set. Observed values of DT yield are shown by straight vertical lines in the figures. Because the simulator is not perfect, the distribution medians do not always agree with the constraining yield data to within $2\sigma_{\text{obs}}$, but all discrepancies are smaller than $\sim 8\%$. This level of disagreement might result from violations of the assumptions of the 1D single-fluid simulator, including shot-to-shot variations in 2D or 3D effects of laser drive asymmetry and the capsule mount, or temperature non-equilibrium among fuel species. Distributions are quite similar with or without ZPKZ,

perhaps because of the choice of composition that would minimize species separation, i.e., D:T = 95:5. The posterior distribution do not include sampling from the observational uncertainty because it is so small.

Figure 11 shows similar comparisons for the volume-averaged time-averaged DT-burn-rate-weighted ion temperature of the four calibration shots, which is obtained directly from the simulations, but observationally is inferred from thermal Doppler broadening of the observed DT neutron spectra. Here the agreement between data and the posterior distributions is quite good, perhaps partly because the observational uncertainty of 0.5 keV is rather large. The posterior distributions including sampling from the observational uncertainty, regarded as a Gaussian with standard deviation σ_{obs} , as well as MCMC sampling of the emulator.

To make predictions about the seven new shots using DTH or DT³He fuel, which were not part of the calibration set, GPM/SA

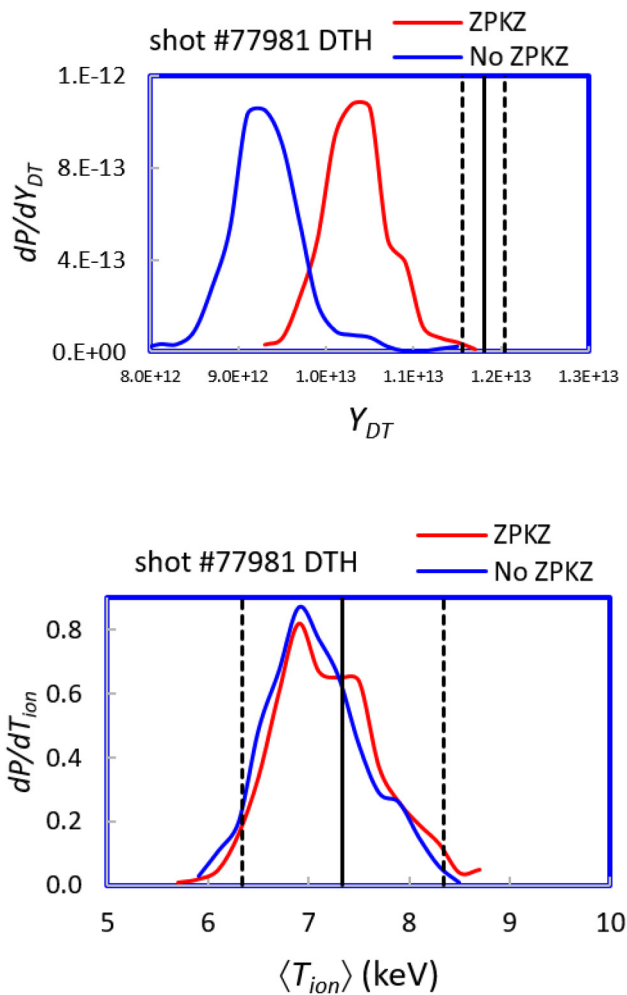


FIG. 12. Posterior predictive distributions (red and blue curves) for DT yield (upper) and average DT ion temperature (lower) for shot #77981, containing DTH. Data are indicated by black vertical lines, showing observed value $\pm 2\sigma_{\text{obs}}$. Yield data give a clear indication of the inverse Rygg effect, compared to the No-ZPKZ prediction, at the level of $\sim 27\% \pm 7\%$. Median and 95% confidence bounds for predicted DT ion temperature are 7.08 (+1.19, -1.08) keV without ZPKZ and 7.17 (+1.09, -0.91) keV with ZPKZ, compared to 7.34 ± 1 keV observed.

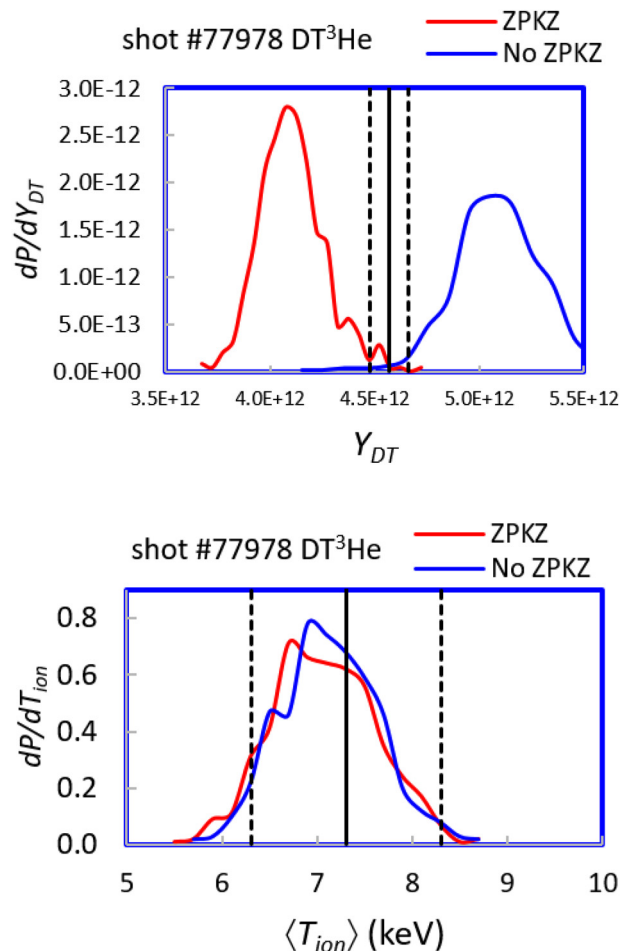


FIG. 13. Posterior predictive distributions (red and blue curves) for DT yield for shot #77978, containing DT³He. Data (black vertical lines, showing observed yield $\pm 2\sigma_{\text{obs}}$) indicate a small Rygg effect, decreasing the yield by about 10%. The ZPKZ prediction gives a larger decrease than observed. Mean and 95% confidence bounds for predicted DT ion temperature are 7.11 (+1.10, -1.05) keV without ZPKZ, and 6.96 (+1.22, -1.03) keV with ZPKZ, compared to 7.31 ± 1 keV observed.

evaluates the integral in Eq. (12), determining the likelihood $P(y(x^*)|\theta)$ by sampling an emulator based on simulations of these shots, and using for $P(\theta|y(x))$ the probability distribution of the input parameters determined as just described, whose projections are shown in Fig. 9. The predictions for these shots are predictions only in the sense that their data were not used to constrain the emulator; in fact, these simulations were carried out well after the time when the experiments were actually conducted.

Figure 12 shows the posterior predictive distributions, with and without ZPKZ, for the DT yield and burn-averaged DT ion temperature of shot #77981, which contained DTH fuel. The observed yield is $27\% \pm 7\%$ higher than the DT yield predicted without ZPKZ, where the uncertainty represents 1σ . We therefore conclude that the experiment shows strong evidence for the “inverse Rygg effect,” at a level of $\sim 4\sigma_{\text{pred}}$. The ZPKZ prediction is higher than the prediction without ZPKZ, because of the inverse Rygg effect in the simulation, but the effect is not as strong as observed; the observed yield is still about 15% higher than the DT yield predicted using ZPKZ. Some of the observed

yield increase can be explained by the fact that the observed DT ion temperature is also higher than the median predictions, as Fig. 12 (lower) shows. Comparing the observed temperature (7.34 keV) to the median temperature predicted without ZPKZ (7.08 keV) and finding from the Bosch-Hale fusion reactivity²⁹ that $\langle \sigma v \rangle \sim T_i^3$ in this regime, we conclude that about 12%, or not quite half, of the 27% inverse-Rygg yield increase might come from the higher observed temperature, while the balance might plausibly come from species separation.

Figure 13 shows the posterior predictive distribution, with and without ZPKZ, for the DT yield of shot #77978, which contained DT³He fuel. The data show the Rygg effect, a decrease in DT yield, but only by about $(10 \pm 5)\%$ (1σ uncertainty), not much larger than the residual discrepancy between the emulator and calibration data exhibited in Fig. 10. The ZPKZ prediction also shows a Rygg-effect decrease in the yield compared to the no-ZPKZ prediction, but here the effect is larger than observed, so that the ZPKZ yield is reduced below the observation. The observed yield is about 12% higher than the DT yield predicted using ZPKZ. In this case, the fact that the observed DT burn

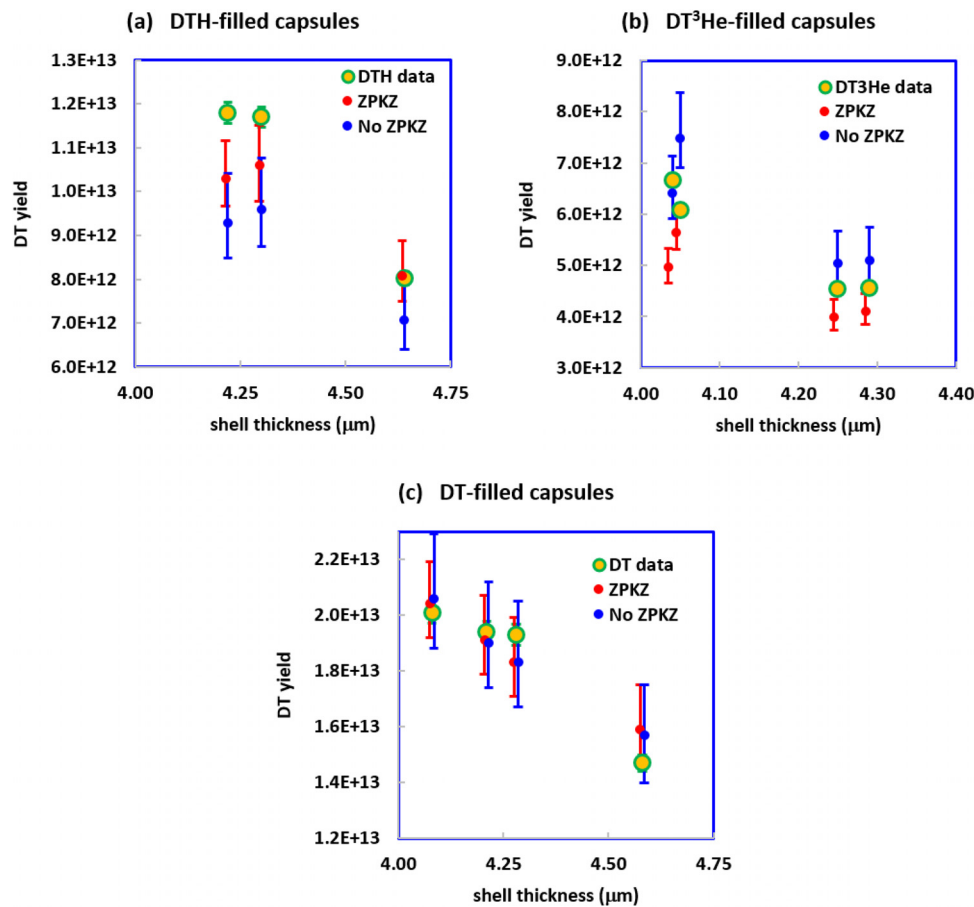


FIG. 14. Comparison of observed DT yield (green yellow-filled circles) with median of posterior predictive probability distributions from GPM/SA analysis, without ZPKZ ion diffusion (blue dots) or with ZPKZ ion diffusion (red dots). Error bars show 95% confidence intervals, or about $\pm 2\sigma_{\text{pred}}$. (a) DTH-filled capsules. Averaging over all three capsules, the observed yield is 1.21 ± 0.04 times larger than the yield predicted without ion diffusion, demonstrating the inverse Rygg effect. (b) DT³He-filled capsules. Averaging over all four capsules, the observed yield is 0.91 ± 0.02 times smaller than the yield predicted without ion diffusion, demonstrating the Rygg effect. (c) DT-filled capsules used as the calibration set. In (a) and (b), occasional close agreement between simulations and data are probably fortuitous, and may result from uncontrolled variations in experimental conditions, such as beam power and target position, affecting yield as much as $\pm 10\%$.

temperature is slightly higher than predicted obviously cannot explain why the observed DT yield is slightly lower than predicted, leaving species separation as a more plausible explanation. In fact, species separation would have to be all the stronger to overcome the yield increase from the higher observed temperature.

The patterns displayed in Figs. 12 and 13 persist in the behavior of the other DTH- and DT^3He -filled shots, as shown in Fig. 14. Here the median and 95% confidence bounds of each posterior predictive distribution are indicated by a point with error bars. Figure 14(a) shows that the observed DT yield of DTH shots is always larger than the no-ZPKZ prediction, implying that our observation of the inverse Rygg effect is robust. Averaging the inverse-Rygg yield increase factor over the three DTH shots, with each measurement weighted inversely by its uncertainty, gives finally the value 1.21 ± 0.04 for the inverse Rygg effect in the present experiment, agreeing well with the value 1.17 ± 0.15 derived above using the hydrodynamic equivalence assumption. In Fig. 14(b), the observed DT yield of DT^3He shots is smaller than the no-ZPKZ prediction in three out of four cases, giving moderately good evidence for the Rygg effect although it is rather small. Averaging the Rygg-yield factor over all four DT^3He shots gives the value 0.91 ± 0.02 for the Rygg effect. This value differs by 2σ from the value 0.65 ± 0.13 derived above using the hydrodynamic equivalence assumption. The difference might result from the relatively strong decrease in burn temperature predicted by the simulator for three of the four DT^3He shots, possibly resulting from composition-dependent variations in ion thermal conductivity, even without species separation, which decreases the predicted DT yield to

near the observed value. But because the observed temperature is not as low as predicted, it is likely that the relative role of species separation, compared to yield reduction resulting from low temperature, is more important in the experiment than in the simulations; i.e., the simulator is “right,” within 9%, for the wrong reasons.

The main difference between the seven DTH and DT^3He shots and the DT calibration shots is in their gas composition, so we conclude with high confidence that some effect associated with the composition, such as ion diffusion and species separation, and/or ion thermal conductivity or ion temperature equilibration, is operating in a way that is not correctly calculated in the no-ZPKZ simulations. Even if ion diffusion is accounted for by using ZPKZ, the capsules’ behavior is not completely explained although the effect of ZPKZ is in the correct direction for six out of seven DTH and DT^3He shots. The experiment was carefully designed so as to limit the range of possible hypotheses to explain the observations, and thus ion species physics is a main candidate.

To get more insight into why ZPKZ simulations do not agree better with observations, we show in Fig. 15 radial profiles of mass density, deuterium/tritium number ratio, and hydrogen/tritium number ratio, at several times around bang time for a simulation of DTH shot #77981, using ZPKZ. As described in the caption, both hydrogen and deuterium are depleted in the fuel relative to tritium at bang time, by ion thermodiffusion, according to the simulation. But, as described above, the DT yields predicted using ZPKZ are smaller than observed for six out of the seven DTH and DT^3He shots. A straightforward interpretation of this fact is that perhaps ZPKZ is causing too much

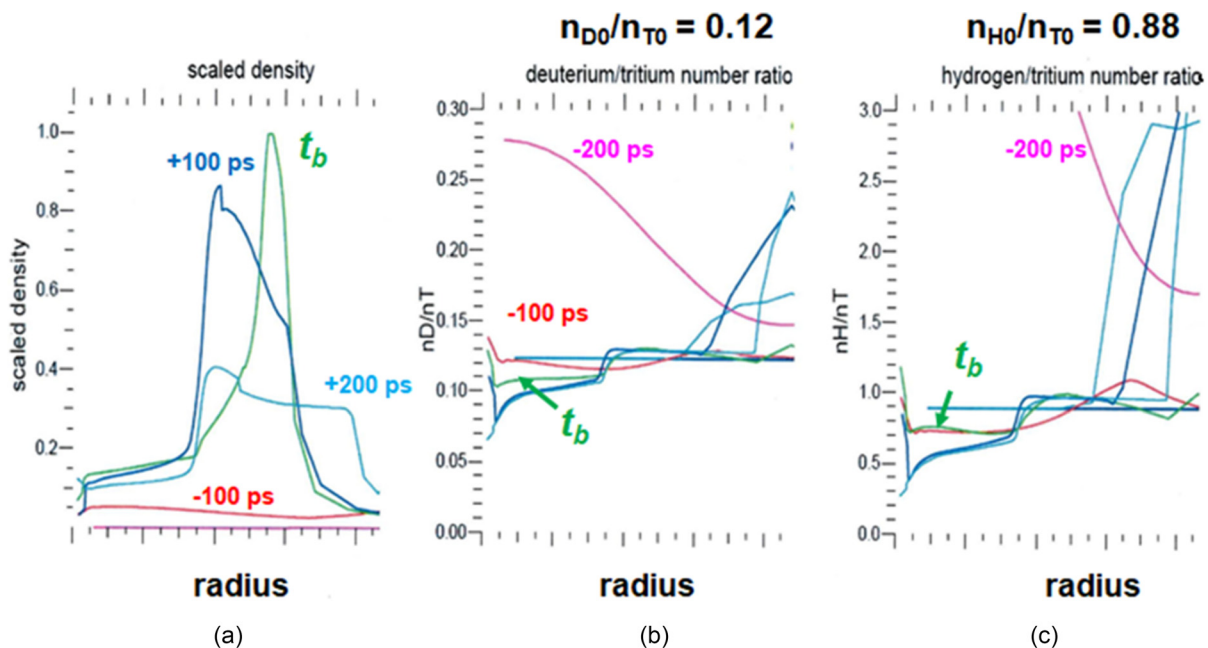


FIG. 15. Radial profiles of (a) mass density, (b) deuterium/tritium number ratio, and (c) hydrogen/tritium number ratio near bang time, in a simulation of shot #77981, which had initial fuel composition $\text{H}/\text{D}/\text{T} = 44/6/50$. In all three panels, the profile 200 ps before bang time is shown as a magenta curve, 100 ps before bang time is shown as a red curve, bang time is shown as a green curve, while dark blue and light blue curves show 100 and 200 ps after bang time, respectively. In (a), the fuel occupies the volume in which scaled density < 0.2 , while the shell has scaled density > 0.2 . In (b), the initial ratio of deuterium to tritium number density is $6/50 = 0.12$. The converging shock compresses the deuterium ahead of the tritium at -200 ps by barodiffusion, causing enhanced deuterium fraction at the core. But later, as the fuel compresses, the ion-temperature gradient causes thermodiffusion to expel deuterium from the fuel, relative to tritium, depressing the deuterium/tritium ratio below 0.12 by bang time, to 0.10–0.11, and even lower later on. In (c), we see similar effects for hydrogen, depressing the hydrogen/tritium ratio from its initial value of $44/50 = 0.88$ to around 0.7 by bang time, and as low as 0.5 later on.

diffusion of D out of the capsule core. Since the observed yields are higher than the ZPKZ median yields by an average of about 13%, it may be that the deuterium mass in the core at bang time is too small by about the same amount, since DT yield is proportional to the product of deuterium fraction and tritium fraction.

The over-depletion of deuterium might in turn result from the assumption of temperature equilibrium between D and T in the single-fluid simulation code, leading to deuterium ion temperatures that are too high. Diffusivity D_i scales sensitively with ion temperature as $T_i^{5/2}$, so, assuming that diffusive flux scales as $D_i^{1/2}$, the mass of deuterium lost by the capsule core scales as $T_i^{5/4}$, so 13% excess deuterium loss could be explained by a deuterium temperature that is about 10% too high. If this is so, then the problem might not lie so much with ZPKZ as with the single-fluid temperature-equilibrium assumption of the underlying hydrodynamics method. Some new ion-transport models are being developed that are more general than ZPKZ. A new model being developed by Klem and Zimmerman³⁰ represents the individual species as separate but coupled fluids, each fluid having its own ion temperature and velocity. Another model due to Kagan and coworkers avoids the assumption in ZPKZ of an ideal plasma, applicable only when the plasma is rarefied and hot enough. Instead, the new model³¹ is applicable to both ideal and non-ideal cases by including the ion coupling effects in the transport calculation. In particular, by using this extended approach, thermodiffusion is predicted to vanish as the density increases.³² Since thermodiffusion is one of the key players conjectured to be responsible for the D over-depletion in the current simulations, using the non-ideal framework should limit the yield reduction compared to the ZPKZ-based calculations, thus bringing them closer to the experimental observations. It will be interesting to test these new models using the data from our experiment.

VI. CONCLUSION

Motivated by previous hydrodynamically-equivalent $D^3\text{He}$ (Ref. 2) and non-hydrodynamic-equivalent DT^3He (Ref. 3) studies, we have developed an implosion platform with four fuel species in three mixtures such as 95/5 DT, DTH, and DT^3He to study multi-fuel effects on implosion dynamics. From both x-ray self-emission images and areal density (fuel and ablator) diagnostics results, it has been shown that three types of hydro-equivalent capsules (DT, DTH, and DT^3He) have similar hydrodynamic compression behavior. However, nuclear yield deviation was observed from the scaling determined using analytic fusion yield formula. In the DT^3He mixture, a reduced yield (i.e., a factor of 0.65 ± 0.13 below scaling prediction) was observed, whereas a yield increase (i.e., a factor of 1.17 ± 0.15 above prediction) was observed in the DTH mixture, supporting the inverse Rygg effect. In addition, the observed DD/DT yield ratio from the DT^3He mixture was about a factor of 0.8 lower than the simulated DD/DT. The DD/DT yield being lower than expected suggests that lighter and less charged D diffuses away from the core and leaves T or ^3He enhanced in the core, supporting the inter-species ion diffusion theory. Alternatively, this observation may indicate that D temperatures are too high in the simulations, compared to the experiment. The DT yield increase observed, compared to scaling, in the DTH mixture is consistent with the inter-species ion diffusion theory where lighter H diffuses away from the core and concentrated DT in the core allows more yield to be produced. In the current DTH mixture with a 5% D concentration, the yield ratio measurement (i.e., TT/DT) was

not achieved because the large background from DT neutron yield interfered with the TT yield. Future DTH experiments using a reduced D initial concentration (e.g., <5% D) will be needed to further study the TT/DT yield ratio. An inter-species ion diffusion model, the Zimmerman–Paquette–Kagan–Zhdanov (ZPKZ) model, implemented in a Lagrangian radiation-hydrodynamics fluid code, was also used to analyze the present data, without the need to assume hydrodynamic equivalence of the capsules. ZPKZ accounts for species separation in multicomponent plasmas. According to the ZPKZ simulations, both hydrogen and deuterium are depleted in the fuel relative to tritium at bang time, by ion thermodiffusion. But the ZPKZ-predicted DT yields are about 13% lower than observed, on average, so it seems that the simulations give somewhat too much deuterium depletion, which may again indicate that, compared to the experiment, D temperatures are too high in these single-fluid simulations, where D and T are forced to be in temperature equilibrium. The simulation-based analysis led to independent estimations of the Rygg-effect yield decrease factor (0.91 ± 0.02 for the DT^3He capsule) and the inverse-Rygg yield increase factor (1.21 ± 0.04 for the DTH capsule), based on simulations that ignored ion diffusion, without assuming hydrodynamic equivalence of the capsules.

ACKNOWLEDGMENTS

The authors acknowledge the support of the OMEGA Laser Facility operations team at Laboratory for Laser Energetics. This work was performed by the Los Alamos National Laboratory, operated by Triad National Security, LLC for the National Nuclear Security Administration (NNSA) of U.S. Department of Energy (DOE) under Contract No. 89233218CNA000001.

APPENDIX A: GAS PRESSURE AT SHOT TIME

Gas pressures at shot time were also in good agreement with requested fill pressures within 96%–114%. In the original manuscript, Table I only showed the as-shot gas pressures (or gas

TABLE IV. Gas pressures at shot time.

	Requested pressure (atm)	Fill pressures to compensate leak (atm)	Pressures at shot time (atm)	$100 \times (\text{pressure at shot time}) / (\text{requested pressure})$
DT 95/5 fill				
D ₂	8.9	8.93–8.98	$8.84 \pm 0.4\%$	99.3%
T ₂	0.5	0.485–0.49	$0.48 \pm 0.4\%$	96%
DTH fill				
D ₂	0.5	0.57–0.58	$0.57 \pm 0.4\%$	114%
T ₂	4.7	4.66–4.69	$4.63 \pm 0.4\%$	98.5%
H ₂	4.2	4.15–4.17	$4.1 \pm 0.4\%$	98%
DT^3He fill				
D ₂	3.58	3.58–3.61	$3.54 \pm 0.2\%$	98.9%
T ₂	0.5	0.5–0.51	$0.493 \pm 0.2\%$	98.6%
³ He	7.1	8.1	$7.12 \pm 8\%$	101.1%

pressures at shot time). We have added the table in the appendix to show the requested pressures, fill pressures (over-pressured to compensate leak), and the percentage of as-shot pressures to requested pressures.

APPENDIX B: LINEAR UNCERTAINTY ANALYSIS FOR EXPECTED YIELD

This appendix gives a brief description of how the fractional uncertainties in observed/expected yield ratios were calculated in Tables II and III. The expected DT yields are given in Eqs. (3), (5), and (8) for the DT, DTH, and DT³He mixture, respectively. In order to perform a linear uncertainty analysis,³³ Eqs. (3), (5), (8) are approximated by its first-order Taylor-series expansion, assuming small variations of the input variables. For example, a fractional uncertainty of Eq. (5) (the expected DT yield from the DTH mixture) is approximated by the following equation, where Δx represents the uncertainty in the variable x. For example, r_{xray} is a radius of imploded capsule and burn width is shown as τ_{burn}

$$\begin{aligned} \left[\frac{\Delta Y_{DT}^{DTH}}{Y_{DT}^{DTH}} \right]^2 &= \left[\frac{\Delta f_D^{DTH}}{f_D^{DTH}} \right]^2 + \left[\frac{\Delta f_T^{DTH}}{f_T^{DTH}} \right]^2 + \left[2 \frac{\Delta \rho^{DTH}}{\rho^{DTH}} \right]^2 \\ &+ \left[2 \frac{\Delta \bar{m}^{DTH}}{\bar{m}^{DTH}} \right]^2 + \left[\frac{\Delta \langle \sigma v(T_i) \rangle^{DTH}}{\langle \sigma v(T_i) \rangle^{DTH}} \right]^2 \\ &+ \left[3 \frac{\Delta r_{xray}^{DTH}}{r_{xray}^{DTH}} \right]^2 + \left[\frac{\Delta \tau_{burn}^{DTH}}{\tau_{burn}^{DTH}} \right]^2. \end{aligned} \tag{B1}$$

Table V lists input variables and their random or statistical uncertainty. In this uncertainty analysis, we only include statistical uncertainty and do not include systematic one because systematic uncertainty will be canceled out in the ratio of (Y_{DT}^{DTH}/Y_{DT}^{DT})_{expected} or (Y_{DT}^{DT³He}/Y_{DT}^{DT})_{expected}.

Gas pressures and resultant fractions by atom were carefully recorded over the course of the experiment. A permeation half-life of each glass shell was measured individually by General Atomics. We selected all 11 capsules which have a half-life around 150 days

TABLE V. Input variables and their random uncertainty used for expected DT yields.

	Fractional uncertainty (%) in DTH	Fractional uncertainty (%) in DT	Fractional uncertainty (%) in DT ³ He	Weighting factor	Contribution in DTH (%)	Contribution in DT (%)	Contribution in DT ³ He (%)
f _D	0.8	0.7	7.9	1	0.8	0.7	7.9
f _T	0.8	0.7	7.9	1	0.8	0.7	7.9
f _H	0.8	0.0	0.0	0	0.0	0.0	0.0
f _{3He}	0.0	0.0	11.3	0	0.0	0.0	0.0
ρ	0.8	0.4	4.5	2	1.6	0.8	9.0
m̄	0.1	0.1	0.7	2	0.2	0.2	1.4
T _i	2.7	1.8	3.2	0	0.0	0.0	0.0
⟨σv(T _i)⟩	8.4	5.4	9.3	1	8.4	5.4	9.3
r _{xray}	2.0	1.0	2.0	3	6.0	3.0	6.0
τ _{burn}	3.2	4.9	7.7	1	3.2	4.9	7.7
Total (%)	11.0	8.0	19.8

at room temperature. During the course of fill and transport, shells were kept in a cryo-container to minimize leakage of fuels. As a result, D₂, T₂, and H₂ pressures at shot time have a small uncertainty less than 1%. ³He was an outlier due to its short half-life of approximately 3 hours at room temperature. The time delay between taking a ³He target out of a ³He-pressurized cell and the actual shot time were limited to less than 30 min and recorded the delay time individually. Uncertainty in the ³He concentration was still relatively large (i.e., 11.3% uncertainty in the ³He concentration in DT³He mixture).

A burn-averaged ion temperature (T_i) was measured by using two nToF detectors: one located at 15.8 m and the other at 12 m. A total uncertainty in T_i is ±0.5 keV, which was influenced by both systematic and statistical uncertainty. The statistical or random shot-to-shot uncertainty in T_i is much smaller. Assuming that the hydro-equivalent implosion is isotropic and of T_i should be the same in different lines of sights, we calculated the ratio of two detector signals (15.8 m nTOF/12 m TOF) for 11 shots. The standard deviation for the T_i ratio was 2.7% during DTH shots, 1.8% in DT shots, and 3.2% in DT³He shots. These results are the random statistical uncertainty (precision) in the T_i measurements used in Tables II and III. Then, uncertainty shown by s in a DT fusion reactivity is calculated as

$$s_{\langle \sigma v(T_i) \rangle} = \frac{\langle \sigma v(\bar{T}_i + s_{T_i}) \rangle - \langle \sigma v(\bar{T}_i - s_{T_i}) \rangle}{2}. \tag{B2}$$

Using this formula, uncertainty in the DT fusion reactivity is 8.4% for DTH, 5.4% for DT, and 9.3% for DT³He. Similarly, the shot-to-shot uncertainty from x-ray emission radius (r_{xray}) was determined by taking a ratio of two GMXI-C (with 75 μm of Al filter) and GMXI-D (with 100 μm of Al filter) detector channels. The standard deviation of the ratio of two channel was also minimal and has 2% in DTH, 1% in DT, and 2% in DT³He. For a shot-to-shot uncertainty in burn width (τ_{burn}), NTD and GCD detectors were used and the standard deviation of the ratio of NTD to GCD was 3.2% in DTH, 4.9% in DT, and 7.7% in DT³He.

Tables VI and VII show an example of the how uncertainty in the expected DT yields propagates through column G to L as

TABLE VI. Uncertainties propagation on 77 981 DTH capsule.

	Contribution of Column G in Table II	Contribution of Column H in Table II	Contribution of Column I in Table II	Contribution of Column J in Table II	Contribution of Column K in Table II	Contribution of Column L in Table II
$[f_D f_T (\rho/\bar{m})^2]^{DTH}$	2.0
$[f_D f_T (\rho/\bar{m})^2]^{DT} / \sqrt{2}$	0.9
$[f_D f_T (\rho/\bar{m})^2 \langle \sigma v(T_i) \rangle]^{DTH}$...	8.3
$[f_D f_T (\rho/\bar{m})^2 \langle \sigma v(T_i) \rangle]^{DT} / \sqrt{2}$...	3.9
$[f_D f_T (\rho/\bar{m})^2 \langle \sigma v(T_i) \rangle r_{xray}^3]^{DTH}$	10.3
$[f_D f_T (\rho/\bar{m})^2 \langle \sigma v(T_i) \rangle r_{xray}^3]^{DT} / \sqrt{2}$	4.4
$[f_D f_T (\rho/\bar{m})^2 \langle \sigma v(T_i) \rangle r_{xray}^3 \tau_{burn}]^{DTH}$	10.8	...	10.8
$[f_D f_T (\rho/\bar{m})^2 \langle \sigma v(T_i) \rangle r_{xray}^3 \tau_{burn}]^{DT} / \sqrt{2}$	5.6	...	5.6
$(Y_{DT}^{DTH})_{observed} / (Y_{DT}^{DT})_{observed}$	1.3	1.3
Total (%)	2.2	9.2	11.2	12.1	1.3	12.1

TABLE VII. Uncertainties propagation on 77 978 DT³He capsule.

	Contribution of Column G in Table III	Contribution of Column H in Table III	Contribution of Column I in Table III	Contribution of Column J in Table III	Contribution of Column K in Table III	Contribution of Column L in Table III
$[f_D f_T (\rho/\bar{m})^2]^{DT^3He}$	14.4
$[f_D f_T (\rho/\bar{m})^2]^{DT} / \sqrt{2}$	0.9
$[f_D f_T (\rho/\bar{m})^2 \langle \sigma v(T_i) \rangle]^{DT^3He}$...	17.4
$[f_D f_T (\rho/\bar{m})^2 \langle \sigma v(T_i) \rangle]^{DT} / \sqrt{2}$...	3.9
$[f_D f_T (\rho/\bar{m})^2 \langle \sigma v(T_i) \rangle r_{xray}^3]^{DT^3He}$	18.4
$[f_D f_T (\rho/\bar{m})^2 \langle \sigma v(T_i) \rangle r_{xray}^3]^{DT} / \sqrt{2}$	4.4
$[f_D f_T (\rho/\bar{m})^2 \langle \sigma v(T_i) \rangle r_{xray}^3 \tau_{burn}]^{DT^3He}$	20.0	...	20.0
$[f_D f_T (\rho/\bar{m})^2 \langle \sigma v(T_i) \rangle r_{xray}^3 \tau_{burn}]^{DT} / \sqrt{2}$	5.6	...	5.6
$(Y_{DT}^{DT^3He})_{observed} / (Y_{DT}^{DT})_{observed}$	1.3	1.3
Total (%)	14.4	17.8	18.9	20.7	1.3	20.7

corrections progress. Specifically, Table VI uses a 77981 shot number as an example for DTH capsules and Table VII uses a 77978 shot number as an example for DT³He capsules.

DATA AVAILABILITY

The data that support the findings of this study are available from the corresponding author upon reasonable request.

REFERENCES

¹J. D. Lindl, P. Amendt, R. Berger, S. G. Glendinning, S. H. Glenzer, S. W. Hann, R. L. Kauffman, O. L. Landen, and L. J. Suter, "The physics basis for ignition using indirect-drive targets on the National Ignition Facility," *Phys. Plasmas* **11**, 339 (2004).
²J. R. Rygg, J. A. Frenje, C. K. Li, F. H. Seguin, R. D. Petrasso, J. A. Delettrez, V. Yu Glebov, V. N. Goncharov, D. D. Meyerhofer, S. P. Regan, T. C. Sangster,

- and C. Stoeckl, "Tests of the hydrodynamic equivalence of direct-drive implosions with different D₂ and ³He mixtures," *Phys. Plasmas* **13**, 052702 (2006).
- ³H. W. Herrmann, J. R. Langenbrunner, J. M. Mack, J. H. Cooley, D. C. Wilson, S. C. Evans, T. J. Sedillo, G. A. Kyrala, S. E. Caldwell, C. S. Young, A. Nobile, J. Wermer, S. Paglieri, A. M. McEvoy, Y. Kim, S. H. Batha, C. J. Horsfield, D. Drew, W. Garbett, M. Rubery, V. Yu Glebov, S. Roberts, and J. A. Frenje, "Anomalous yield reduction in direct-drive deuterium/tritium implosions due to ³He addition," *Phys. Plasmas* **16**, 056312 (2009).
- ⁴H. G. Rinderknecht, P. A. Amendt, S. C. Wilks, and G. Collins, "Kinetic physics in ICF: Present understanding and future directions," *Plasma Phys. Controlled Fusion* **60**, 099601 (2018).
- ⁵W. T. Taitano, A. N. Simakov, L. Chacon, and B. Keenan, "Yield degradation in inertial-confinement-fusion implosions due to shock-driven kinetic fuel-species stratification and viscous heating," *Phys. Plasmas* **25**, 056310 (2018).
- ⁶S. C. Hsu, T. R. Joshi, P. Hakel, E. L. Vold, M. J. Schmitt, N. M. Hoffman, R. M. Rauenzahn, G. Kagan, X.-Z. Tang, R. C. Mancini, Y. Kim, and H. W. Herrmann, "Observations of interspecies ion separation in inertial-confinement-fusion implosions," *EPL* **115**, 65001 (2016).
- ⁷T. R. Joshi, P. Hakel, S. C. Hsu, E. L. Vold, M. J. Schmitt, N. M. Hoffman, R. M. Rauenzahn, G. Kagan, X.-Z. Tang, R. C. Mancini, Y. Kim, and H. W. Herrmann, "Observations and modeling of interspecies ion separation in inertial-confinement-fusion implosions via imaging x-ray spectroscopy," *Phys. Plasmas* **24**, 056305 (2017).
- ⁸T. R. Joshi, S. C. Hsu, P. Hakel, N. M. Hoffman, H. Sio, and R. C. Mancini, "Progress on observations of interspecies ion separation in inertial-confinement-fusion implosions via imaging x-ray spectroscopy," *Phys. Plasmas* **26**, 062702 (2019).
- ⁹A. Le, T. J. T. Kwan, M. J. Schmitt, H. W. Herrmann, and S. H. Batha, "Simulation and assessment of ion kinetic effects in a direct-drive capsule implosion experiment," *Phys. Plasmas* **23**, 102705 (2016).
- ¹⁰P. Amendt, O. L. Landen, H. F. Robey, C. K. Li, and R. D. Petrasso, "Plasma barodiffusion in inertial-confinement-fusion implosions: Application to observed yield anomalies in thermonuclear fuel mixtures," *Phys. Rev. Lett.* **105**, 115005 (2010).
- ¹¹G. Kagan and X. Tang, "Thermo-diffusion in inertially confined plasmas," *Phys. Lett. A* **378**, 1531 (2014).
- ¹²G. Kagan and X. Tang, "Electro-diffusion in a plasma with two ion species," *Phys. Plasmas* **19**, 082709 (2012).
- ¹³P. Amendt, S. C. Wilks, C. Bellei, C. K. Li, and R. D. Petrasso, "The potential role of electric fields and plasma barodiffusion on the inertial confinement fusion database," *Phys. Plasmas* **18**, 056308 (2011).
- ¹⁴N. B. Meezan, L. F. Berzak Hopkins, S. Le Pape, L. Divol, A. J. MacKinnon, T. Doppner, D. D. Ho, O. S. Jones, S. F. Khan, T. Ma, J. L. Milovich, A. E. Pak, J. S. Ross, C. A. Thomas, L. R. Benedetti, D. K. Bradley, P. M. Celliers, D. S. Clark, J. E. Field, S. W. Haan, N. Izumi, G. A. Kyrala, J. D. Moody, P. K. Patel, J. E. Ralph, J. R. Rygg, S. M. Sepke, B. K. Spears, R. Tommasini, R. P. J. Town, J. Biener, R. M. Bionta, E. J. Bond, J. A. Caggiano, M. J. Eckart, M. Gatu Johnson, G. P. Grim, A. V. Hamza, E. P. Hartouni, R. Hatarik, D. E. Hoover, J. D. Kilkenny, B. J. Koziolowski, J. J. Kroll, J. M. McNaney, A. Nikroo, D. B. Sayre, M. Stadermann, C. Wild, B. E. Yoxall, O. L. Landen, W. W. Hsing, and M. J. Edwards, "Cryogenic tritium-hydrogen-deuterium and deuterium-tritium layer implosions with high density carbon ablaters in near-vacuum hohlraums," *Phys. Plasmas* **22**, 062703 (2015).
- ¹⁵D. T. Casey, J. A. Frenje, M. Gatu Johnson, M. J.-E. Manuel, H. G. Rinderknecht, N. Sinenian, F. H. Seguin, C. K. Li, R. D. Petrasso, P. B. Radha, J. A. Delettrez, V. Yu Glebov, D. D. Meyerhofer, T. C. Sangster, D. P. McNabb, P. A. Amendt, R. N. Boyd, J. R. Rygg, H. W. Herrmann, Y. H. Kim, and A. D. Bacher, "Evidence for stratification of deuterium-tritium fuel in inertial confinement fusion implosions," *Phys. Rev. Lett.* **108**, 075002 (2012).
- ¹⁶T. R. Boehly, D. L. Brown, R. S. Craxton, R. L. Keck, J. P. Knauer, J. H. Kelly, T. J. Kessler, S. A. Kumpan, S. J. Loucks, S. A. Letzring, F. J. Marshall, R. L. McCrory, S. F. B. Morse, W. Seka, J. M. Soures, and C. P. Verdon, "Initial performance results of the OMEGA laser system," *Opt. Commun.* **133**, 495 (1997).
- ¹⁷F. J. Marshall and J. A. Oertel, "A framed monochromatic x-ray microscope for ICF (invited)," *Rev. Sci. Instrum.* **68**, 735 (1997).
- ¹⁸C. K. Li, F. H. Seguin, D. G. Hicks, J. A. Frenje, K. M. Green, S. Kurebayashi, and R. D. Petrasso, "Study of direct-drive, deuterium-tritium gas-filled plastic capsule implosions using nuclear diagnostics at OMEGA," *Phys. Plasmas* **8**, 4902 (2001).
- ¹⁹M. S. Rubery, C. J. Horsfield, S. G. Gales, W. J. Garbett, A. Leatherland, C. Young, H. Herrmann, Y. Kim, N. M. Hoffman, J. M. Mack, R. Aragonéz, T. Sedillo, S. Evans, R. B. Brannon, C. Stoeckl, J. Ulreich, A. Sorce, G. Gates, M. J. Shoup III, B. Peck, M. Gatu Johnson, J. A. Frenje, J. S. Milnes, and W. Stoeffl, "First measurement of remaining shell areal density on the OMEGA laser using the diagnostic for areal density (DAD)," *Rev. Sci. Instrum.* **89**, 083510 (2018).
- ²⁰Y. Kim, H. W. Herrmann, N. M. Hoffman, M. J. Schmitt, P. A. Bradley, S. Gales, C. J. Horsfield, M. Rubery, A. Leatherland, M. Gatu Johnson, J. A. Frenje, and V. Yu Glebov, "Direct-drive DT implosions with Knudsen number variations," *J. Phys. Conf. Ser.* **717**, 012030 (2016).
- ²¹M. Gittings, R. Weaver, M. Clover, T. Betlach, N. Byrne, R. Coker, E. Dendy, R. Hueckstaedt, K. New, W. R. Oakes, D. Ranta, and R. Stefan, "The RAGE radiation-hydrodynamic code," *Comput. Sci. Discovery* **1**(1), 015005 (2008).
- ²²D. Higdon, J. Gattiker, B. Williams, and M. Rightley, "Computer model calibration using high-dimensional output," *J. Am. Stat. Assoc.* **103**, 570 (2008).
- ²³D. Osthus, S. A. Vander Wiel, N. M. Hoffman, and F. J. Wysocki, "Prediction uncertainties beyond the range of experience: A case study in inertial confinement fusion implosion experiments," *SIAM/ASA J. Uncertainty Quantif.* **7**, 604-633 (2019).
- ²⁴A. B. Zylstra, N. M. Hoffman, H. W. Herrmann, M. J. Schmitt, Y. H. Kim, K. Meaney, A. Leatherland, S. Gales, C. Forrest, V. Yu Glebov, M. Schoff, M. Hoppe, and N. Ravelo, "Diffusion-dominated mixing in moderate convergence implosions," *Phys. Rev. E* **97**, 061201(R) (2018).
- ²⁵G. Dimonte, "Spanwise homogeneous buoyancy-drag model for Rayleigh-Taylor mixing and experimental evaluation," *Phys. Plasmas* **7**, 2255 (2000).
- ²⁶N. M. Hoffman, G. B. Zimmerman, K. Molvig, H. G. Rinderknecht, M. J. Rosenberg, B. J. Albright, A. N. Simakov, H. Sio, A. B. Zylstra, M. Gatu Johnson, F. H. Seguin, J. A. Frenje, C. K. Li, R. D. Petrasso, D. M. Higdon, G. Srinivasan, V. Yu. Glebov, C. Stoeckl, W. Seka, and T. C. Sangster, "Approximate models for the ion-kinetic regime in inertial-confinement-fusion capsule implosions," *Phys. Plasmas* **22**, 052707 (2015).
- ²⁷C. Paquette, C. Pelletier, G. Fontaine, and G. Michaud, "Diffusion coefficients for stellar plasmas," *Astrophys. J. Suppl. Ser.* **61**, 177 (1986).
- ²⁸V. M. Zhdanov, "Transport processes in multicomponent plasma," *Plasma Phys. Controlled Fusion* **44**, 2283 (2002).
- ²⁹H.-S. Bosch and G. M. Hale, "Improved formulas for fusion cross-sections and thermal reactivities," *Nucl. Fusion* **32**, 611 (1992).
- ³⁰D. Klem and G. Zimmerman, "Multiple ion temperatures," Lawrence Livermore National Laboratory Report No. LLNL-TR-752184, 2018.
- ³¹G. Kagan and S. D. Baalrud, "Transport formulas for multi-component plasmas within the effective potential theory framework," [arXiv:1611.09872](https://arxiv.org/abs/1611.09872) (2018).
- ³²G. Kagan, S. D. Baalrud, and J. Daligault, "Influence of coupling on thermal forces and dynamic friction in plasmas with multiple ion species," *Phys. Plasmas* **24**, 072705 (2017).
- ³³N. M. Hoffman, H. W. Herrmann, Y. H. Kim, H. H. Hsu, C. J. Horsfield, M. S. Rubery, E. K. Miller, E. Grafil, W. Stoeffl, J. A. Church, C. S. Young, J. M. Mack, D. C. Wilson, J. R. Langenbrunner, S. C. Evans, T. J. Sedillo, V. Yu Glebov, and T. Duffy, "Measurement of areal density in the ablaters of inertial-confinement-fusion capsules via detection of ablator (n, n' γ) gamma-ray emission," *Phys. Plasmas* **20**, 042705 (2013).